Structure of the Lifeact–F-actin complex

Alexander Belyy[1], Felipe Merino[1,2], Oleg Sitsel[1] and Stefan Raunser[1*]

[1]Department of Structural Biochemistry, Max Planck Institute of Molecular Physiology, Otto-Hahn-Str. 11, 44227 Dortmund, Germany

[2]Current address: Department of Protein Evolution, Max Planck Institute for Developmental Biology, Max-Planck-Ring 5, 72076, Tübingen, Germany.

*Correspondence should be addressed to: stefan.raunser@mpi-dortmund.mpg.de

Abstract

Lifeact is a short actin-binding peptide that is used to visualize filamentous actin (F-actin) structures in live eukaryotic cells using fluorescence microscopy. However, this popular probe has been shown to alter cellular morphology by affecting the structure of the cytoskeleton. The molecular basis for such artefacts is poorly understood. Here, we determined the high-resolution structure of the Lifeact–F-actin complex using electron cryo-microscopy. The structure reveals that Lifeact interacts with a hydrophobic binding pocket on F-actin and stretches over two adjacent actin subunits, stabilizing the DNase I-binding loop of actin in the closed conformation. Interestingly, the hydrophobic binding site is also used by actin-binding proteins, such as cofilin and myosin and actin-binding toxins, such as TccC3HVR from *Photorhabdus luminescens* and ExoY from *Pseudomonas aeruginosa*. *In vitro* binding assays and activity measurements demonstrate that Lifeact indeed competes with these proteins, providing an explanation for the altering effects of Lifeact on cell morphology *in vivo*. Finally, we demonstrate that the affinity of Lifeact to F-actin can be increased by introducing mutations into the peptide, laying the foundation for designing improved actin probes for live cell imaging.

Introduction

The network of actin filaments in eukaryotic cells is involved in processes ranging from intracellular trafficking to cell movement, cell division and shape control (Pollard and Cooper, 2009). It is therefore not surprising that much effort has been directed to characterize the actin cytoskeleton under both physiological and pathological conditions. Numerous actin-visualizing compounds were developed to enable this. These include small molecules, labelled toxins, recombinant tags, as well as actin-binding proteins and peptides (see (Melak et al., 2017) for a detailed review). However, using these molecules to study actin *in vivo* often alters the properties of actin filaments to such an extent that normal homeostasis of the cytoskeleton is impaired. Since these side effects cannot be avoided, it is important to know their molecular basis in order to be able to adequately interpret the experimental data.

Phalloidin and jasplakinolide are cyclic peptides derived from the death cap mushroom *Amanita phalloides* and marine sponge *Jaspis johnstoni* (Crews et al., 1986; Lynen and Wieland, 1938), respectively. They bind specifically to F-actin, and when fused to a fluorescent probe their derivatives allow visualization of the cell cytoskeleton by fluorescence microscopy (Melak et al., 2017). However, both molecules strongly stabilize F-actin and shift the cellular actin equilibrium, largely limiting their use in live cell imaging (Bubb et al., 2000; Dancker et al., 1975). Recent cryo-EM studies from our group and others have uncovered how phalloidin and jasplakinolide affect the structure of F-actin and described the potential limitations of their use (Mentes et al., 2018; Merino et al., 2018a; Pospich et al., 2019).

The development of various fluorescent proteins provided new ways of visualizing the actin cytoskeleton. A simple and popular technique compatible with live cell imaging is to express actin fused to GFP-like proteins (Ballestrem et al., 1998). However, such actin chimeras often interfere with the normal functionality of the cytoskeleton in a way that results in experimental artefacts (Aizawa et al., 1997; Nagasaki et al., 2017). An alternative to GFP-actin is to fuse GFP to actin-binding proteins, such as utrophin (Burkel et al., 2007; Lin et al., 2011) or *Arabidopsis* fimbrin (Sheahan et al., 2004) and synthetic affimers that bind actin (Kost et al., 1998; Lopata et al., 2018). These actin filament markers have been successfully used in a variety of cell types and organisms (Melak et al., 2017; Montes-Rodriguez and Kost, 2017; Spracklen et al., 2014).

The most recent development is an F-actin binding nanobody called Actin-Chromobody that claims to have a minimal effect on actin dynamics and no notable effect on cell viability (Schiavon et al., 2019). However, the binding of the Actin-Chromobody to actin has not yet been characterized at molecular level, leaving the true extent of possible side effects open.

As described above, fluorophore-bound proteins are large and bulky resulting in possible steric clashes when interacting with actin. To avoid these problems, small fluorophore-labeled peptides were developed. The most commonly used one is Lifeact, which is a 17 amino acid peptide derived from the N-terminus of the yeast actin-binding protein ABP140. In the original publication, Lifeact was described as a novel F-actin probe that does not interfere with actin dynamics *in vitro* and *in vivo* (Riedl et al., 2008). The same group later reported transgenic Lifeact-GFP expressing mice that were phenotypically normal and fertile (Riedl et al., 2010), and no influence of Lifeact on cellular processes was found under the published experimental conditions. Two other groups performed a direct comparison of various F-actin binding probes and confirmed the low influence of Lifeact on cell cytoskeletal architecture (Belin et al., 2014; Sliogeryte et al., 2016). Later on, however, several major Lifeact-caused artefacts were described: Lifeact was unable to stain certain F-actin rich structures (Munsie et al., 2009; Sanders et al., 2013), it disturbed actin assembly in fission yeast (Courtemanche et al., 2016), it caused infertility and severe actin defects in *Drosophila* (Spracklen et al., 2014), and altered cell morphology in mammalian cells (Flores et al., 2019). The existing explanatory hypothesis suggests that Lifeact induces a conformational change in F-actin that affects binding of cofilin and eventually impairs cell cytoskeletal dynamics (Courtemanche et al., 2016). However, despite the widespread usage of Lifeact, the validity of this hypothesis is still a matter of debate since no structure of Lifeact-decorated F-actin has been available.

In order to address this, we solved the structure of the Lifeact–F-actin complex using single particle cryo-EM. The 3.5 Å structure reveals that Lifeact binds to the two consecutive actin subunits of the same strand of the filament and displaces the DNase I-binding loop (D-loop) upon binding. The binding site overlaps with that of cofilin and myosin, suggesting that artefacts in live-cell imaging are caused by competition between these proteins and Lifeact. Competition binding assays *in vitro* prove that this is indeed the case. Furthermore, we show that the binding of Lifeact to F-actin considerably reduces the *in vivo* toxicity of the actin-modifying toxin TccC3HVR from *Photorhabdus luminescens*. Our data will help to predict potential artefacts in experiments using Lifeact, and will serve as a strong basis for developing new actin-binding probes with improved properties.

Results and Discussion

Structure of the Lifeact–F-actin complex

Based on previous studies (Mentes et al., 2018; Merino et al., 2018b; Pospich et al., 2019), we know that phalloidin stabilizes actin filaments. When it is added during polymerization, the nucleotide binding pocket is occupied with an ADP and P_i and the D-loop is in the open conformation (Pospich et al., 2019). We therefore polymerized actin in the presence of phalloidin and added an excess of Lifeact to the formed filaments in order to fully decorate the filaments with Lifeact. We then determined the structure of this complex by cryo-EM (Fig. 1, Table 1). The average resolution of the reconstruction was 3.5 Å, with local areas reaching 3.0 Å (Fig. S1), which allowed us to build an atomic model in which we could position most of the side chains. We could clearly identify densities corresponding to ADP, Mg^{2+} and P_i in the nucleotide-binding pocket of actin (Fig. 1A) and a density corresponding to phalloidin at the expected position (Mentes et al., 2018; Merino et al., 2018a; Pospich et al., 2019) in the center of the filament (Fig. 1A). Lifeact was well resolved and we could unambiguously fit 16 out of 17 amino acids into the density (Fig. 1, Fig. S2).

The peptide folds as an α-helix and spans two consecutive actin subunits of the same strand of the filament (Fig. 1A, B). The binding pocket is formed by the tip of the D-loop of the lower subunit (M47) and SD1 of the upper subunit, where the N-terminal region of Lifeact is almost locked in by the protruding D25 of actin (Fig. 1B). Although Lifeact is in general a hydrophilic peptide, it contains a hydrophobic patch formed by the side chains of V3, L6, I7, F10 and I13 which all orient to one side. This hydrophobic patch interacts with a hydrophobic groove on the surface of F-actin which comprises M44, M47, Y143, I345 and L349. F10 of Lifeact is deeply buried in this pocket (Fig. 1C). Interestingly and contrary to what we have seen before in samples co-polymerized with phalloidin (Pospich et al., 2019), the D-loop is in its closed conformation (Fig. S3). A comparison between the Lifeact-F-actin-ADP-P_i -phalloidin- structure with that of phalloidin-stabilized F-actin-ADP-P_i (Pospich et al., 2019) shows that direct interactions between Lifeact and the D-loop of F-actin are only possible if the D-loop is in its closed conformation (Movie S1). Specifically, I13 of Lifeact interacts with M47 of F-actin, stabilizing the closed D-loop conformation in F-actin. This suggests that Lifeact has a higher affinity to F-actin-ADP, where the D-loop is in the closed conformation, than to phalloidin-stabilized F-actin-ADP-P_i, where the D-loop has to be first moved from the open to the closed conformation. Indeed, Kumari *et al.* (Kumari et al., 2019) showed in a complementary study that the affinity of Lifeact is three to four times higher for F-actin-ADP compared to F-actin-ADP-P_i.

Properties of the interaction site

Guided by the insights gained from our structure, we mutated different residues at the peptide-actin interface to study the binding properties of Lifeact in more detail. We chose to use *Saccharomyces cerevisiae* for these studies since actin mutagenesis can be easily and rapidly performed in this organism. To avoid toxicity from artificial overexpression of Lifeact, we expressed Lifeact-mCherry under the promoter of the actin binding protein ABP140 from which Lifeact was originally derived, and then performed confocal microscopy experiments to visualize Lifeact-actin interaction.

When expressing WT Lifeact-mCherry, we observed the typical patch morphology of actin-rich structures that are distinct from the diffuse background of Lifeact-mCherry. These actin-rich patches can also be observed when the cells are stained by fluorescently-labelled phalloidin (Fig. 2A). However, when L6 was mutated to lysine, or F10 to alanine, we did not observe these structures and Lifeact-mCherry was homogeneously distributed in the cells. Although the I13A variant displayed some of the patches, they were significantly less abundant than with WT Lifeact-mCherry (Fig. 2A, B). While the Lifeact L6K mutant introduces a charge in the hydrophobic patch, Lifeact mutants F10A and I13A retain the hydrophobicity but change the surface structure of the peptide. Since all mutations impaired the interaction between actin and Lifeact, we conclude that hydrophobicity as well as shape complementarity are important for efficient Lifeact binding to F-actin.

Our structure suggests that actin D25 acts as an N-terminal cap for the helix of Lifeact and a mutation of actin D25 to tyrosine would affect this interaction and mutating L349 of actin to methionine would impair its crucial interaction with Lifeact F10. Indeed, actin-rich structures were also absent when Lifeact-mCherry was expressed in cells with the D25Y or the L349M actin variant (Fig. 2C, D), indicating that actin D25 and Lifeact F10 are important for Lifeact binding.

To study the effect of Lifeact WT and variants on yeast viability we overexpressed Lifeact-MBP fusions under a strong galactose promoter and analyzed their toxicity in a yeast growth phenotype assay. Consistent with a previously reported study (Courtemanche et al., 2016), we observed that the overexpression of Lifeact-MBP caused cell toxicity (Fig. 2E). However, mutagenesis of I13 to alanine improved, and L6 to lysine and F10 to alanine fully restored yeast growth. Altogether, these results demonstrate the importance of shape complementarity as well as hydrophobicity at the Lifeact-actin interface.

Lifeact mutations increase its affinity to F-actin

Despite these specific interactions between Lifeact and F-actin, the peptide binds to F-actin only with micromolar affinity (Riedl et al., 2008). A higher affinity would provide a stronger signal-to-noise ratio, decreasing the background during live imaging, and allowing lower expression levels of the peptide to be used during such experiments. We therefore attempted to increase the affinity of Lifeact to F-actin by structure-guided *in silico* design using RosettaScripts (Fleishman et al., 2011) based on our atomic model. The simulation output suggested several possible mutations after residue 12 of Lifeact (Fig. 3A). The mutation E16R was especially promising. It was predicted to add an additional interaction with the D-loop and an electrostatic interaction with E167 of actin (Fig. 3B). Indeed, this variant showed an increased affinity for F-actin as judged by cosedimentation assays (Fig. 3C, D). Although we could not observe density for E17 of Lifeact in our density map, we also created and tested a E17K variant of Lifeact which should similarly create an additional interaction with E167 of actin and thereby increase the affinity of the peptide. In line with the prediction, E17K Lifeact-MBP variants showed an increased affinity for F-actin (Fig. 3C, D). Together, these modifications show that based on our atomic model, Lifeact can be optimized by mutations to increase its binding to actin.

Lifeact competes with cofilin and myosin

Several studies demonstrated that Lifeact staining interfered with cofilin binding to actin. It was shown that Lifeact does not bind to cofilin-bound F-actin in cells (Munsie et al., 2009) and Lifeact-expressing cells possess longer and thicker stress fibers. Studies by Flores *et al.* (Flores et al., 2019) suggested that reduced cofilin binding to F-actin is the underlying cause of the observed Lifeact-induced artefacts. Similarly, Lifeact caused changes in endocytosis and cytokinesis of *Schizosaccharomyces pombe*, which were attributed to reduced cofilin interaction with actin (Courtemanche et al., 2016). The authors of that study proposed that cofilin and Lifeact bind to different regions of F-actin, and suggested that binding of one of these proteins impairs binding of the other by provoking a conformational change in F-actin (Courtemanche et al., 2016).

Apart from Lifeact-induced stabilization of the closed conformation of the D-loop, however, our structure does not show major differences to previously reported structures of F-actin (Merino et al., 2018b; Pospich et al., 2019). Therefore, a conformational change in F-actin cannot be the cause for the effect of Lifeact. When comparing our F-actin–Lifeact structure with that of F-actin–cofilin (Tanaka et al., 2018), it becomes obvious that the binding site of

cofilin overlaps with that of Lifeact (Fig. 4A). Notably, the same is true for myosin, which interacts with the same position on the actin surface (Fig. 4B) (Ecken et al., 2016). We therefore performed *in vitro* competition actin binding assays with human cofilin-1, the motor domain of human non-muscle myosin 2C isoform (NM2C), and Lifeact. Lifeact successfully decreased cofilin and myosin binding in a dose-dependent manner (Fig. 4C-F). As a negative control, we performed a similar competition assay with tropomyosin that binds to a different region of actin (Fig. 4G) (Ecken et al., 2015), and the Lifeact F10A mutant which only binds weakly to F-actin (Fig. 4C-F). As expected, the addition of Lifeact did not affect tropomyosin binding to F-actin (Fig. 4H, I), nor could F10A Lifeact compete with cofilin-1 or NM2C (Fig. 4C-F). Based on our structural and functional data, we demonstrate that the morphological artefacts described for Lifeact are not due to a conformational change in actin but are caused by competition for the same binding site on F-actin of Lifeact with actin-binding proteins, such as cofilin and myosin.

Lifeact impairs the activity of bacterial toxins

In our laboratory, we study two bacterial toxins that interact with F-actin. One is *Pseudomonas aeruginosa* ExoY, a toxin that becomes a potent nucleotidyl cyclase upon interaction with F-actin (Belyy et al., 2016). After activation, the toxin generates a supraphysiologic amount of cGMP and cAMP that impedes cell signaling. It was previously demonstrated that the mutagenesis of D25 in actin abolishes ExoY binding to F-actin (Belyy et al., 2018). The same actin mutation also prevents Lifeact binding, we therefore hypothesize that Lifeact and ExoY have overlapping binding sites.

The second toxin is the 30 kDa C-terminal fragment of *Photorhabdus luminescens* TccC3 (TccC3HVR), which is the effector domain of the large Tc toxin complex PTC3. Once it is translocated into the cell by the injection machinery of PTC3, TccC3HVR acts as an ADP-ribosyltransferase that modifies actin at T148 (Lang et al., 2010). This leads to uncontrolled actin polymerization, clustering, and finally to cell death due to cytoskeletal collapse. T148 is located in close proximity to the Lifeact binding site, therefore the actin binding site of TccC3HVR and Lifeact might overlap.

To understand whether Lifeact competes with the binding of ExoY, we first performed a cosedimentation assay with ExoY, F-actin and different concentrations of Lifeact. In agreement with our hypothesis, we observed a decrease of ExoY binding to F-actin in the presence of Lifeact while the Lifeact F10A mutant did not impair formation of the ExoY-F-actin complex (Fig. 5A, B).

We then ADP-ribosylated F-actin by TccC3HVR in the presence of Lifeact. In our experimental setup, 3 µM of WT Lifeact was already sufficient to decrease the level of ADP ribosylation by a factor of two, while in the control reaction 100 µM of F10A Lifeact did not decrease the level of ADP-ribosylation at all (Fig. 5C, D). This experiment strongly supports the hypothesis that TccC3HVR and Lifeact bind to the same region of F-actin.

Encouraged by these *in vitro* results, we decided to test whether expressing Lifeact in mammalian cells would protect them from the TccC3HVR toxin. We therefore expressed either mCherry-tagged WT Lifeact, Lifeact F10A, Lifeact E17K, or mCherry-tagged actin as a negative control in adherent HEK 293T cells. We then intoxicated the cells with PTC3 and observed the effect of the injected TccC3HVR. Our control cells expressing actin and cells expressing the F-actin binding-incompetent F10A Lifeact showed rapid cytoskeletal collapse and accompanying overall shrinkage (Fig. 5E, F). However, the toxic effect of TccC3HVR was significantly reduced in cells that expressed WT Lifeact or the binding-competent E17K mutant. Thus, Lifeact has anti-toxin properties and despite its effects on the cytoskeleton, it has the potential to be used as a precursor for the development of anti-toxin drugs.

Conclusions

In this study we determined the binding site of Lifeact on F-actin and demonstrated that this peptide directly competes with actin-binding proteins such as cofilin and myosin, providing an explanation for how Lifeact alters cell morphology. In addition, we demonstrate how the affinity of Lifeact can be modulated by site directed mutagenesis in order to create Lifeact-based probes with modified properties. Our results have strong implications for the usage of Lifeact as an actin filament label in fluorescent light microscopy and provide cell biologists with the background information that is needed to make a properly informed decision on whether to use Lifeact in an experiment. Furthermore, we have demonstrated that Lifeact competes with actin-binding toxins such as ExoY and TccC3HVR, and partially counteracts the intoxication of cells by PTC3 toxin. This paves the way for the development of Lifeact-based anti-toxin drugs.

Materials and methods

Plasmids, bacteria and yeast strains, growth conditions

The complete list of used oligonucleotides, constructions and strains can be found in the Supplementary data. *E. coli* strains were grown in LB medium supplemented with ampicillin (100 µg/ml) or kanamycin (50 µg/ml). *S. cerevisiae* were grown on rich YPD medium or on synthetic defined medium (Yeast nitrogen base, Difco) containing galactose or glucose and supplemented if required with uracil, histidine, leucine, tryptophan, or adenine. *S. cerevisiae* strains were transformed using the lithium-acetate method (Daniel Gietz and Woods, 2002). Yeast actin mutagenesis was performed as described previously (Belyy et al., 2015). Yeast viability upon Lifeact-MBP overexpression under the galactose promoter was analyzed by a drop test: 5-fold serial dilutions of cell suspensions were prepared from overnight agar cultures by normalizing OD_{600} measurements, then spotted onto agar plates and incubated for 2-3 days at 30 °C. Analysis of protein expression in yeast was performed following the described protocol (Kushnirov, 2000): yeast cells were grown in liquid galactose-containing medium overnight at 30 °C. Cells corresponding to 1 ml of OD_{600} 1.0 were washed with 0.1 M NaOH, resuspended in 50 µl of 4-fold Laemmli sample buffer, and boiled for 5 minutes at 95 °C. 5 µl of the extracts were separated by SDS-PAGE, followed by Western blotting analysis and incubation with anti-MBP (NEB), anti-actin (C4, Abcam) or anti-RPS9 serum (polyclonal rabbit antibodies were a generous gift of Prof. S. Rospert).

Protein expression and purification

Fusion proteins of Lifeact variants or *Pseudomonas aeruginos*a ExoY toxin and maltose-binding protein (MBP) were purified from *E. coli* BL21-CodonPlus(DE3)-RIPL cells harboring the corresponding plasmids (2489 pB502 WT Lifeact-MBP, 2490 pB506 E16R Lifeact-MBP, 2491 pB524 E17K Lifeact-MBP, 2479 pB386 MBP-ExoY). A single colony was inoculated in 100 ml of LB media and grown at 37 °C. At OD_{600} 1.0 protein expression was induced by addition of IPTG to a final concentration of 1 mM. After 2 h of expression at 37 °C, the cells were harvested by centrifugation, resuspended in buffer A (20 mM Tris pH 8, 500 mM NaCl), and lysed by sonication. The soluble fraction was applied on buffer A-equilibrated Protino Ni-IDA resin (Macherey-Nagel), washed, and eluted by buffer A, supplemented with 250 mM imidazole. Finally, the eluates were dialyzed against buffer B (20 mM Tris pH 8, 150 mM NaCl) and stored at -20 °C.

Rabbit skeletal muscle α-actin was purified as described previously (Merino et al., 2018b) and stored in small aliquots at -80 °C.

Human cofilin-1 was purified from *E. coli* cells using previously described method (Carlier et al., 1997). In short, Rosetta DE3 *E. coli* cells were transformed with the 1855 plasmid. An overnight culture derived from a single colony was diluted into 2 L of LB media to OD_{600} 0.06 and grown at 37 °C. When OD_{600} reached 0.7, the cells were cooled to 30 °C and cofilin expression was induced by adding IPTG to a final concentration of 0.5 mM. After 4 h of expression, the cells were harvested by centrifugation, resuspended in buffer C (10 mM Tris pH 7.8, 1 mM EDTA, 1 mM PMSF and 1 mM DTT), and lysed using a fluidizer. The soluble fraction of the lysate was dialyzed overnight in buffer D (10 mM Tris pH 7.8, 50 mM NaCl, 0.2 mM EDTA and 2 mM DTT), and cleared by centrifugation. Then, the lysate was applied onto DEAE resin and washed with buffer D. Cofilin-containing fractions of the flow-through were collected and dialyzed against buffer E (10 mM PIPES pH 6.5, 15 mM NaCl, 2 mM DTT and 0.2 mM EDTA). After centrifugation, the protein was loaded onto Mono S cation exchange column and eluted by a linear gradient of 15 mM to 1 M NaCl in buffer E. Cofilin-containing fractions were concentrated to 10 mg/ml and stored at -80 °C.

Human tropomyosin was purified from *E. coli* BL21(DE3) cells transformed with a 1609 plasmid using the previously described method (Coulton et al., 2006) with minor modifications. In brief, an overnight culture derived from a single colony was diluted into 5 L of LB media to OD_{600} 0.06 and grown at 37 °C. When the OD_{600} reached 0.5, the cells were cooled down to 20 °C and recombinant protein expression was induced by adding IPTG to a final concentration of 0.4 mM. After overnight protein expression, the cells were harvested by centrifugation, resuspended in buffer F (20 mM Tris pH 7.5, 100 mM NaCl, 5 mM $MgCl_2$, 2 mM EGTA and Roche cOmplete protease inhibitor) and lysed by fluidizer. The soluble fraction of the lysate was heated for 10 minutes at 80 °C, then cooled down to 4 °C and centrifuged. The supernatant was mixed 1:1 with buffer H (20 mM sodium acetate buffer pH 4.5, 100 mM NaCl, 5 mM $MgCl_2$ and 2 mM EGTA). The precipitate was collected and incubated for 1 h with buffer I (10 mM Bis-Tris pH 7, 100 mM NaCl). The renatured protein was applied to a HiTrap Q anion exchange column and eluted by a linear gradient of 100 mM to 1 M NaCl in buffer I. Tropomyosin-containing fractions were pooled and stored at -80 °C.

The motor domain of non-muscular myosin-2C (MYH14, isoform 2 from *H. sapiens*) consisting of amino acids 1–799 was purified as described previously (Ecken et al., 2016)

Tcc3HVR, the ADP-ribosyltransferase domain of the *Photorhabdus luminescens* TccC3 protein (amino acids 679 - 960) was purified as described previously (Roderer et al., 2019).

The TcdA1 and TcdB1-TccC3 components of the *Photorhabdus luminescens* PTC3 toxin were expressed and purified as described previously (Gatsogiannis et al., 2016).

320

321 **Cryo-EM sample preparation, data acquisition, and processing**

322 Actin was polymerized by incubation in F-buffer in the presence of a twofold molar excess of
323 phalloidin for 30 minutes at room temperature and further overnight at 4 °C. The next day, actin
324 filaments were pelleted using a TLA-55 rotor for 30 minutes at 150.000 g at 4 °C and
325 resuspended in F-buffer. 5 minutes before plunging, F-actin was diluted to 6 µM and mixed
326 with 200 µM Lifeact peptide (the peptide of sequence MGVADLIKKAESISKEE with C-
327 terminal amide modification was provided by Genosphere with >95% purity. The peptide was
328 dissolved in 10 mM Tris pH 8). To improve ice quality, Tween-20 was added to the sample to
329 a final concentration of 0.02% (w/v). Plunging was performed using the Vitrobot Mark IV
330 system (Thermo Fisher Scientific) at 13 °C and 100% humidity: 3 µl of sample were applied
331 onto a freshly glow-discharged copper R2/1 300 mesh grid (Quantifoil), blotted for 8 s on both
332 sides with blotting force -20 and plunge-frozen in liquid ethane.

333 The dataset was collected using a Talos Arctica transmission electron microscope
334 (Thermo Fisher Scientific) equipped with an XFEG at 200 kV using the automated data-
335 collection software EPU (Thermo Fisher Scientific). Two images per hole with defocus range
336 of -0.6 - -3.35 µm were collected with the Falcon III detector (Thermo Fisher Scientific)
337 operated in linear mode. Image stacks with 40 frames were collected with total exposure time
338 of 3 sec and total dose of 60 e^-/Å. 1415 images were acquired and 915 of them were further
339 processed. Filaments were automatically selected using crYOLO (Wagner et al., 2019).
340 Classification, refinement and local resolution estimation were performed in SPHIRE (Moriya
341 et al., 2017). Erroneous picks were removed after a round of 2D classification with ISAC. After
342 removing bad particles, further segments were removed to ensure that each filament consists of
343 at least 5 members. After 3D refinement, particles were polished using Bayesian polishing
344 routine in Relion (Zivanov et al., 2018) and refined once again within SPHIRE.

345

346 **Model building and design**

347 We used the structure of actin in complex with ADP-Pi (PDBID 6FHL) as starting model for
348 the filament, and built a *de novo* model of the Lifeact peptide using Rosetta's fragment-based
349 approach (Wang et al., 2015). Since one residue of Lifeact is missing from the density, we
350 threaded the sequence in all possible registers – including the reverse orientations – and
351 minimized them in Rosetta. The solution starting from M1 with the N-terminus pointing
352 towards the pointed end was clearly better than all the others (Fig. S2). A set of restraints for
353 phalloidin were built with eLBOW (Moriarty et al., 2009) and the toxin was manually fit into

the density with Coot (Emsley et al., 2010). The model was further refined using iterative rounds of Rosetta's fragment-based iterative refinement (DiMaio et al., 2015), and manual building with Coot and ISOLDE (Croll, 2018; Emsley et al., 2010). The model was finally refined within Phenix (Liebschner et al., 2019) to fit B-factors and correct the remaining geometry errors.

We used RosettaScripts (Fleishman et al., 2011) to design a version of Lifeact with improved affinity. The input protocol and starting files are available upon request. The figures were made using UCSF Chimera (Pettersen et al., 2004).

Yeast confocal microscopy

Yeast cells bearing plasmids that encode Lifeact-mCherry variants under the native ABP140 promoter and terminator, were grown overnight on a liquid synthetic defined medium (Yeast nitrogen base, Difco) supplemented with glucose. On the following day, the cultures were diluted to OD_{600} 0.5 using fresh media, incubated for 2-3 h at 30 °C and centrifuged at 6,000 g. The cell pellet was washed twice with PBS buffer, fixed by 4% formaldehyde for 20 minutes at room temperature, washed once with PBS buffer and stained with the ActinGreen 488 probe (Invitrogen). After 30 minutes incubation with the probe at room temperature, the cells were washed twice in PBS and applied to concanavalin A-coated glass bottom Petri dishes. Image acquisition was performed with a Zeiss LSM 800 confocal laser scanning microscope, equipped with 63X 1.4 DIC III M27 oil-immersion objective and two lasers with wavelengths of 488 and 561 nm. To avoid experimental bias, we measured the weighted colocalization coefficient of phalloidin with Lifeact-mCherry in 15 cells of each strain using ZEN software.

Cosedimentation assays

F-actin was prepared as follows. An aliquot of freshly thawed G-actin was centrifuged at 150,000 g using a TLA-55 rotor for 30 minutes at 4 °C to remove possible aggregates. Then, actin was polymerized by incubation in F-buffer (120 mM KCl, 20 mM Tris pH 8, 2 mM $MgCl_2$, 1 mM DTT and 1 mM ATP) for 2 h at room temperature or overnight at 4 °C. For the cosedimentation experiments with myosin, actin was polymerized in the presence of a twofold molar excess of phalloidin. After polymerization, actin filaments were pelleted using a TLA-55 rotor at 150,000 g for 30 minutes and resuspended in the following buffers: F-buffer was used for cosedimentations with tropomyosin or Lifeact-MBP fusion proteins; 20 mM HEPES pH 6.5, 50 mM KCl, 2 mM $MgCl_2$ was used for cosedimentations with cofilin; 120 mM KCl, 20 mM Tris pH 8, 2 mM $MgCl_2$, 1 mM DTT was used for cosedimentations with myosin.

Cosedimentation assays were performed in 20 µl volumes by first incubating F-actin with the specified proteins for 5 minutes at room temperature, then centrifuging at 150,000 g using the TLA-55 or TLA120.1 rotor for 30 minutes at 4 °C. For the competition assays, Lifeact peptide was added to the mixture at the specified concentrations. After centrifugation, aliquots of the supernatant and resuspended pellet fractions were separated by SDS-PAGE using 4-15% gradient TGX gels (Bio-Rad) and analyzed by densitometry using Image Lab software (Bio-Rad).

ADP-ribosylation of actin by TccC3HVR

8 µl mixtures of 1 µg (2.4 µM) actin and Lifeact peptide at specified concentrations were pre-incubated for 5 minutes at room temperature in TccC3 buffer (1 mM NAD, 20 mM Tris pH 8, 150 mM NaCl and 1 mM $MgCl_2$). The ADP-ribosylation reaction was initiated by addition of 0.02 µg (61 pM) of TccC3HVR into the mixture. After 10 minutes of incubation at 37 °C, the reaction was stopped by adding Laemmli sample buffer and heating the sample at 95 °C for 5 minutes. Components of the mixture were separated by SDS-PAGE, blotted onto a PVDF membrane using a Trans-Blot Turbo transfer system (Bio-Rad) and visualized using a combination of anti-mono-ADP-ribose binding reagent (Merck) and anti-rabbit-HRP antibody (Bio-Rad). The level of actin ADP-ribosylation was quantified by densitometry using Image Lab software (Bio-Rad).

Confocal microscopy of mammalian cells and the *in vivo* intoxication competition assay

0.05 x 10^6 HEK 293T cells were seeded in 35 mm glass-bottom, poly-L-lysine coated Petri dishes in 2 mL DMEM/F12 + 10% FBS media and grown for 24 h in a 5% CO_2 atmosphere at 37 °C. The cells were then transfected with mCherry fusions of actin or Lifeact variants using the FuGENE transfection reagent (Promega). The cells were grown for a further 24 h and transferred to an LSM 800 microscope (Zeiss) equipped with a C-Apochromat 40x/1.2 W objective and maintained in a 5% CO_2 atmosphere at 37 °C. Images were acquired using the Airyscan detector and a 561 nm laser wavelength for excitation. After taking the first image (0 h), 300 pM PTC3 was added (pre-formed by mixing purified TcdA1 and TcdB2-TccC3 in a 5:1 molar ratio). Images were taken at 10-minute intervals for 5 h.

The images were processed in Fiji (Schindelin et al., 2012). The cells were selected by applying a threshold on the red fluorescence channel, then their areas were measured, normalized to the original cell area at the 0 h time point, and the resulting % change in cell area that occurred during the experiment was plotted.

422 Three independent experiments for each construct were performed. The cells were not tested
423 for *Mycoplasma* contamination.
424

Figure legends

Figure 1. Cryo-EM structure of the Lifeact-F-actin-ADP-P_i-phalloidin complex. A: The 3.5 Å resolution map of the Lifeact-F-actin-ADP-P_i-phalloidin complex shows a defined density for phalloidin (cyan), ADP-P_i (gold) and the Lifeact peptide (green). The central subunit of actin is colored in orange while its surrounding four neighbors are shown in red. **B**: Atomic model of the interface between Lifeact and F-actin. **C**: Surface of the atomic model of F-actin colored according to its hydrophobicity. Hydrophobicity increases as the color scale goes from white to gold. The inset highlights the hydrophobic nature of the Lifeact-binding surface.

Figure 2. The Lifeact–F-actin complex is affected by point mutations. A, C: Confocal microscopy images of yeast cells expressing Lifeact-mCherry variants in a WT actin background (**A**) and WT Lifeact-mCherry in yeast with different actin variants (**C**). Actin was additionally stained with fluorescently labeled phalloidin (ActinGreen 488). Representative areas where yeast cells are stained with both fluorophores are shown. Note that for our experiments we used the previously described D25Y/D222G double mutant of yeast actin (Belyy et al., 2016). However, D222 is located in subdomain IV and is therefore unlikely to play a role in the Lifeact–F-actin interaction. Scale bars, 5 μm. **B, D**: Calculated weighted colocalization coefficients of phalloidin with Lifeact-mCherry from 15 yeast cells from two independent experiments with five micrographs each, corresponding to (**A**) and (**C**), respectively. For statistical analysis, the paired *t* test was used. *** $p < 0.001$. The error bars in the panels correspond to standard deviations of three independent experiments. **E**: Growth phenotype assay with yeast overexpressing Lifeact-MBP variants under a strong galactose promoter. The top image marked “Glucose” corresponds to experimental conditions with low Lifeact expression. The central image marked “Galactose” corresponds to experimental conditions with high Lifeact expression. The lower image is a Western blot of cells grown on galactose-containing media performed using anti-MBP, anti-actin and anti-RPS9 antibodies.

Figure 3. Lifeact sequence design. A: Frequency of amino acids in the top 100 designs produced by Rosetta. **B**: Predicted structure of the E16R mutant. The wild-type structure is included for comparison. **C**: Cosedimentation of F-actin and 1 μM Lifeact-MBP proteins detected by SDS-PAGE. The upper band corresponds to Lifeact-MBP, and the lower band corresponds to actin. sup, supernatant; pel, pellet. A representative stain-free gel is shown. **D**: The fractions of Lifeact-MBP that cosedimented with F-actin were quantified by densitometry

458 and plotted versus actin concentrations. The error bars in panel **D** correspond to standard
459 deviations of three independent experiments.
460
461 **Figure 4. Lifeact competes with cofilin and myosin *in vitro*. A, B, G**: Structural models of
462 the (**A**) cofilin–F-actin (PDB 5YU8) (Tanaka et al., 2018), (**B**) myosin–F-actin (PDB 5JLH)
463 (Ecken et al., 2016) and (**G**) tropomyosin–F-actin (3J8A) (Ecken et al., 2015) complexes. **C**:
464 SDS-PAGE analysis of cosedimentation experiments of F-actin (3 µM, upper band) with cofilin
465 (3 µM, lower band) in the presence of the indicated amounts of Lifeact. A representative stain-
466 free gel is shown. **E**: SDS-PAGE analysis of cosedimentation experiments of F-actin (0.7 µM,
467 lower band) with myosin (0.5 µM, upper band) in the presence of the indicated amounts of
468 Lifeact. A representative stain-free gel is shown. **H**: SDS-PAGE analysis of cosedimentation
469 experiments of F-actin (3 µM, lower band) with tropomyosin (3 µM, upper band) in the
470 presence of the indicated amounts of Lifeact. A representative Coomassie stained gel is shown.
471 The fractions of cofilin, myosin and tropomyosin that co-sedimented with F-actin in the
472 corresponding experiments were quantified by densitometry and plotted against Lifeact
473 concentrations at **D**, **F** and **I**, respectively. The error bars in **D**, **F** and **I** correspond to standard
474 deviations of three independent experiments. sup, supernatant; pel, pellet.
475
476 **Figure 5. Lifeact impairs the activity of F-actin binding bacterial toxins. A**: SDS-PAGE
477 analysis of cosedimentation experiments of F-actin (1 µM, lower band) with ExoY-MBP (1
478 µM, upper band) in the presence of the indicated amounts of Lifeact. sup, supernatant; pel,
479 pellet. A representative stain-free gel is shown. The fractions of ExoY that co-sedimented with
480 F-actin were quantified by densitometry and plotted against Lifeact concentrations in **B**. **C**:
481 Level of actin ADP-ribosylation by TccC3HVR in the presence of Lifeact was analyzed by
482 Western blot using an ADP-ribose binding reagent. The equal loading of actin was additionally
483 checked by imaging the same stain-free gel prior to blotting (lower image). The ADP-
484 ribosylation level of actin was quantified by densitometry and plotted against Lifeact
485 concentrations in **D**. Error bars at **B** and **D** correspond to standard deviations of three
486 independent experiments. **E**: HEK 293T cells expressing mCherry fusions of actin or LifeAct
487 variants were intoxicated with 300 pM of the *P. luminescens* toxin PTC3, which injects
488 TccC3HVR into cells. The degree of cytoskeletal collapse and accompanying cell shrinkage
489 was monitored for 5 h using live cell imaging, and is plotted in **F** based on three independent
490 experiments for each condition. Scale bars, 20 µm.
491

Figure S1. Overview of the cryo-EM data. A, B: Example micrograph (**A**) and its power spectrum (**B**) at ~ -1.5 µm defocus. Filaments selected automatically by crYOLO are highlighted as differently colored dots. Scale bar 10 µm. **C**: Density map of the Lifeact-F-actin complex colored according to the local resolution. **D**: Orientation distribution of the particles used in the final refinement round. **E:** Fourier shell correlation (FSC) for the masked and un-masked final reconstructions. The FSC was calculated in the central 120 Å area of the map.

Figure S2. Fit quality of the atomic model of LifeAct. A: Minimized energy of models of all possible registers of the LifeAct sequence into the density. Start1 and 2 correspond to the peptides starting at M1 or G2 with their N-termini pointing towards the pointed end of the filament. For Start1-rev and Start2-rev the N-termini points towards the barbed end. The Rosetta energy values show a clear preferred solution. **B:** Density fit of the final model corresponding to the energy minimum seen in (**A**).

Figure S3. Comparison of D-loop conformations. The density maps and corresponding atomic models of Lifeact-F-actin-ADP-P_i-phalloidin in comparison to those of the open D-loop state in F-actin-ADP-P_i-phalloidin (PDB 6T1Y, EMDB 10363) (Pospich et al., 2019) and closed D-loop state in F-actin-ADP-phalloidin (PDB 6T20, EMDB 10364) (Pospich et al., 2019).

Movie S1. **Stabilization of the D-loop in its closed state upon Lifeact binding. A:** The density map of F-actin-ADP-P_i-phalloidin (EMDB 10363, gray) is superimposed with the corresponding atomic model (PDB 6T20) (Pospich et al., 2019). **B**: Close-up view of the D-loop and the C-terminal interface of F-actin-ADP-P_i-phalloidin complex. Possible position of Lifeact on F-actin-ADP-P_i-phalloidin shown in transparent green. Note that the D-loop is in its open state. **C**: Close-up view on the interface between Lifeact and F-actin-ADP-P_i-phalloidin complex. I13 of Lifeact interacts with M47 of F-actin, stabilizing the closed D-loop conformation in F-actin. **D**: Overview of the complete Lifeact-F-actin-ADP-P_i-phalloidin map and the corresponding atomic model.

Table 1.

Cryo-EM data collection, refinement and validation statistics

Microscopy	
Microscope	Talos Arctica
Voltage (kV)	200
Defocus range (μm)	-0.6 to -3.35
Camera	Falcon III (Linear mode)
Pixel size (Å)	1.21
Total electron dose (e/Å^2)	60
Exposure time (s)	3
Frames per movie	40
Number of images	915 (1,415)
3D Refinement	
Number of helical segments	223,480 (246,423)
Final resolution (Å)	3.5
Map sharpening (Å^2)	-50
Helical rise (Å)	27.3
Helical twist (°)	-167.18
Atomic model statistics	
Non-hydrogen atoms	15575
Molprobity score	0.78
Clashscore	0.91
EMRinger score	3.1
Bond RMSD (Å)	0.0155
Angle RMSD (°)	1.49
Poor rotamers (%)	0.31
Favored rotamers (%)	99.69
Ramachandran favored (%)	98.42
Ramachandran allowed (%)	1.58
Ramachandran outliers (%)	0

Author contribution

A.B. prepared cryo-EM specimens and collected data. F.M. processed cryo-EM data, built the atomic model and design. A.B. performed *in vitro* competition and activity assays, and *in vivo* experiments in yeast. O.S. performed and analyzed intoxication assays in mammalian cells. A.B, F.M. and O.S. prepared figures and video. A.B., F.M. and O.S. wrote the original draft of the manuscript. S.R. supervised the project, reviewed and edited the manuscript. All authors reviewed the results and commented on the manuscript.

Acknowledgements

We thank S. Shydlovskyi for assistance with data collection, O. Hofnagel and D. Prumbaum for maintaining the EM facility, S. Bergbrede and M. Hülseweh for the excellent technical assistance, W. Linke and A. Unger (Ruhr-Universität Bochum, Germany) for providing us with muscle acetone powder, S. Rospert (University of Freiburg, Germany) for providing us anti-RPS9 serum, and S. Pospich for fruitful discussions. This work has been funded by the Max Planck Society (S.R.). A.B. is a fellow of the Humboldt foundation.

Supplementary materials and methods

Table S1. List of primers, strains and plasmids used in this study.

Bacterial and yeast strains	**Description**	**Reference**
E. coli DH5α	F^- Φ80*lacZ*ΔM15 Δ(*lacZYA-argF*) U169 *rec*A1 *end*A1 *hsd*R17(r_k^-, m_k^+) *pho*A *sup*E44 *thi*-1 *gyr*A96 *rel*A1 λ^-	Invitrogen
E. coli BL21 DE3	F^- *ompT hsdS*(r_B^- m_B^-) *gal dcm* (DE3)	Novagen
E. coli BL21 DE3 CodonPlus RIPL	F^- *ompT hsdS*(r_B^- m_B^-) *dcm*$^+$ Tet^r *gal*λ(DE3) *endA* Hte [*argU proL* Cam^r] [*argU ileY leuW* Strep/Spec^r]	Agilent
S. cerevisiae MH272-3fα	"Wild-type" strain, *ura3, leu2, his3, trp1, ade2*	(Peisker et al., 2008)
S. cerevisiae SC483	*S. cerevisiae* MH272-3fα *act1::*LEU2 + *ACT1*[Ura3]	(Belyy et al., 2015)
S. cerevisiae SC489	*S. cerevisiae* MH272-3fα *act1::*LEU2 + *ACT1*[His3]	(Belyy et al., 2015)
S. cerevisiae SC690	*S. cerevisiae* MH272-3fα *act1::*LEU2 + *ACT1* D25Y/D222G[His3]	(Belyy et al., 2016)
S. cerevisiae Y446	*S. cerevisiae* MH272-3fα + empty vector[Ura3] (pESC-Ura)	This study
S. cerevisiae Y453	*S. cerevisiae* MH272-3fα + Lifeact-mCherry[Ade] (2477)	This study
S. cerevisiae Y479	*S. cerevisiae* MH272-3fα *act1::*LEU2 + *ACT1* D25Y/D222G[His3] + Lifeact-mCherry[Ade] (2477)	This study
S. cerevisiae Y484	*S. cerevisiae* MH272-3fα *act1::*LEU2 + *ACT1* L349M[His3] (2478) Strain *S. cerevisiae* SC483 was transformed with plasmid 2478 and passed over 5-FOA to remove WT actin plasmid with Ura3-marker (Belyy et al., 2015)	This study
S. cerevisiae Y497	*S. cerevisiae* MH272-3fα *act1::*LEU2 + *ACT1* L349M[His3] + Lifeact-mCherry[Ade] (2477)	This study
S. cerevisiae Y510	*S. cerevisiae* MH272-3fα + Lifeact-MBP[Ura3] (2481)	This study
S. cerevisiae Y512	*S. cerevisiae* MH272-3fα + Lifeact L6K-MBP[Ura3] (2482)	This study
S. cerevisiae Y513	*S. cerevisiae* MH272-3fα + Lifeact F10A-MBP[Ura3] (2483)	This study
S. cerevisiae Y514	*S. cerevisiae* MH272-3fα + Lifeact I13A-MBP[Ura3] (2484)	This study
S. cerevisiae Y529	*S. cerevisiae* MH272-3fα *act1::*LEU2 + *ACT1*[His3] + Lifeact-mCherry[Ade] (2477)	This study
S. cerevisiae Y552	*S. cerevisiae* MH272-3fα + Lifeact L6K-mCherry[Ade] (2485)	This study
S. cerevisiae Y553	*S. cerevisiae* MH272-3fα + Lifeact F10A-mCherry[Ade] (2486)	This study
S. cerevisiae Y554	*S. cerevisiae* MH272-3fα + Lifeact I13A-mCherry[Ade] (2487)	This study
Plasmids for experiments in *S. cerevisiae*		

2473 YEpGal555	*E. coli*/*S. cerevisiae* shuttle vector [ADE2] with Gal1 promoter	(Belyy et al., 2015)
2474 pESC-Ura	*E. coli*/*S. cerevisiae* shuttle vector [URA3, Amp^r] with Gal1 and Gal10 promoters	Agilent
2475 p1387 pRS313 Actin	*E. coli*/*S. cerevisiae* shuttle vector [HIS3, Ap^r] based on pRS313 vector, containing Act1 gene with native promoter and terminator.	(Belyy et al., 2018)
2476 pB399 pESC-Ura Lifeact-mCherry	The mCherry gene was amplified from 693 using oligonucleotides tatagaattcatggtgagcaagggcgaggag and tataatcgatgacttgtacagctcgtccatgcc. The resulting PCR fragment was digested with EcoRI and ClaI and ligated into digested 2474 pESC-Ura vector.	This study
2477 pB430 YEpGal555 Lifeact-mCherry	DNA fragments containing 5'UTR and the Lifeact-encoding sequence of ABP140 were amplified from genomic DNA of *S. cerevisiae* MH272-3fα strain using oligonucleotides tatagcggccgcagaactgcaccgtacgctcaga and ctcactggcgcgccttcttcctttgagatgctttcg. The 3'UTR of ABP140 was amplified from genomic DNA of *S. cerevisiae* MH272-3fα strain using oligonucleotides gataagatctgaaataggaagttctgagacaagtacc and tatagagctcaaattttatatacacgaaggtg. mCherry was amplified from 2476 using oligonucleotides cttcctatttcagatcttatcgtcgtcatcc and ggaagaaggcgcgccagtgagcaagggcgaggaggataac. Products of these three independent reactions were mixed and amplified with oligonucleotides tatagcggccgcagaactgcaccgtacgctcaga and tatagagctcaaattttatatacacgaaggtg. The final PCR product was digested with NotI and SacI and ligated into digested 2473 YEpGal555 vector.	This study
2478 pB449 pRS313 Actin L349M	The L349M mutation was generated by two-step overlap PCR using oligonucleotides tcttggcttctatgactaccttccaa, caggaaacagctatgacc, ttggaaggtagtcatagaagccaaga and ttcgtgataagtgatagtg. The PCR product was digested with ClaI and SalI and was used to exchange the WT ACT1 gene in 2475 p1387 pRS313 Actin.	This study
2481 pB464 pESC-Ura Lifeact-MBP	The plasmid was constructed in two steps. First, LifeAct-coding sequence was added to 2480 by inserting annealed oligonucleotides catgggtgtcgcagatttgatcaagaaattcgaaagcatctcaaaggaagaagg and taccttcttcctttgagatgctttcgaatttcttgatcaaatctgcgacacc into NcoI/NdeI-digested 2480. Then, the resulting plasmid was used to amplify Lifeact-MBP fragment using oligonucleotides ctttaagaaggagagaattcatgggtgtc and tatacggccggtgatgatgatgatgattgttg. The PCR product was digested with EcoRI and Eco52I, and ligated into digested 2474 pESC-Ura vector.	This study

2482 pB481 pESC-Ura Lifeact L6K-MBP	The plasmid was constructed in two steps. First, LifeAct-coding sequence was added to 2480 by inserting annealed oligonucleotides catgggtgtcgcagataagatcaagaaattcgaaagcatctcaaaggaagaagg and taccttcttcctttgagatgctttcgaatttcttgatcttatctgcgacacc into NcoI/NdeI-digested 2480. Then, the resulting plasmid was used to amplify Lifeact-MBP fragment using oligonucleotides ctttaagaaggagagaattcatgggtgtc and tatacggccggtgatgatgatgatgatgattgttg, digested with EcoRI and Eco52I, and ligated into digested 2474 pESC-Ura vector.	This study
2483 pB482 pESC-Ura Lifeact F10A-MBP	The plasmid was constructed in two steps. First, LifeAct-coding sequence was added to 2480 by inserting annealed oligonucleotides catgggtgtcgcagatttgatcaagaaagccgaaagcatctcaaaggaagaagg and taccttcttcctttgagatgctttcggctttcttgatcaaatctgcgacacc into NcoI/NdeI-digested 2480. Then, the resulting plasmid was used to amplify Lifeact-MBP fragment using oligonucleotides ctttaagaaggagagaattcatgggtgtc and tatacggccggtgatgatgatgatgatgattgttg, digested with EcoRI and Eco52I, and ligated into digested 2474 pESC-Ura vector.	This study
2484 pB483 pESC-Ura Lifeact I13A-MBP	The plasmid was constructed in two steps. First, LifeAct-coding sequence was added to 2480 by inserting annealed oligonucleotides catgggtgtcgcagatttgatcaagaaattcgaaagcgcctcaaaggaagaagg and taccttcttcctttgaggcgctttcgaatttcttgatcaaatctgcgacacc into NcoI/NdeI-digested 2480. Then, the resulting plasmid was used to amplify Lifeact-MBP fragment using oligonucleotides ctttaagaaggagagaattcatgggtgtc and tatacggccggtgatgatgatgatgatgattgttg, digested with EcoRI and Eco52I, and ligated into digested 2474 pESC-Ura vector.	This study
2485 pB516 YEpGal555 Lifeact L6K-mCherry	A DNA fragment encoding Lifeact with the mutation L6K was created from 2477 using oligonucleotides atatagcgcgccttcttcctttgagatgctttcgaatttcttgatcttatctgcg and tatagcggccgcagaactgcaccgtacgctcaga. Then, the PteI and Eco52I-digested PCR-fragment was used to replace WT Lifeact sequence in 2477.	This study
2486 pB517 YEpGal555 Lifeact F10A-mCherry	A DNA fragment encoding Lifeact with the mutation F10A was created from 2477 using oligonucleotides atatagcgcgccttcttcctttgagatgctttcggctttcttg and tatagcggccgcagaactgcaccgtacgctcaga. Then, the PteI and Eco52I-digested PCR-fragment was used to replace WT Lifeact sequence in 2477.	This study
2487 pB518 YEpGal555 Lifeact I13A-mCherry	A DNA fragment encoding Lifeact with the mutation I13A was created from 2477 using oligonucleotides atatagcgcgccttcttcctttgaggcgctttcg and	This study

	tatagcggccgcagaactgcaccgtacgctcaga. Then, the PteI and Eco52I-digested PCR-fragment was used to replace WT Lifeact sequence in 2477.	
Plasmids for protein expression in *E. coli*		
1315 pTriEx4_NMHC2C	The motor domain of non-muscular myosin-2C (MYH14, isoform 2 from *H. sapiens*) consisting of amino acids 1–799	(Ecken et al., 2016)
1609 pET19 tropomyosin	The human tropomyosin alpha-1 gene was synthesized by General Biosystems and cloned into pET19 vector digested with NcoI/BamHI.	This study
1855 cofilin	Human cofilin-1	(Hsiao et al., 2015)
2479 pB386 pET28a MBP-His-ExoY	The ExoY gene was amplified from pUM460 (Belyy et al., 2016) using oligonucleotides tatagagctctggtcgtatcgacggtcatcgtca and tataaagcttcagaccttacgttggaaaaagtc. The resulting PCR product was digested with SacI and HindIII and insterted into pB137 (Belyy et al., 2018) in frame with MBP tag.	This study
2480 pB437 pET28a MBP-His	The MBP gene was amplified from pMAL-c5X (NEB) using oligonucleotides tatacatatgtcgggctcgagcgggagctctggtaaaatcgaagaaggtaaactggtaatctgg and tataggatccttagtgatgatgatgatgattgttgttgttgttcgagctcgaattag. The resulting DNA fragment was digested with NdeI and BamHI and inserted into digested pET28a vector (Novagen).	This study
2488 pB500 pET28a MBP-His-Flag	To increase the size of the carrier protein, a 3x-Flag tag was added to 2480 using PCR and oligonucleotides tatacatatgtcgggctcgagcgggagctctggtaaaatcgaagaaggtaaactggtaatctgg and tataggatccttatttatcatcatcatctttataatcaatatcatgatctttataatcgccatcatgatctttataatc cgaatgatggtgatgatgatgatgattgttgttgttg. The PCR fragment was digested with NdeI and BamHI and inserted into digested pET28a vector (Novagen)	This study
2489 pB502 pET28a Lifeact-MBP-His-Flag	The Lifeact-encoding sequence was generated by annealing oligonucleotides catgggtgtcgcagatttgatcaagaaattcgaaagcatctcaaaggaagaagg and taccttcttcctttgagatgctttcgaatttcttgatcaaatctgcgacacc, and inserting the resulting double-strand DNA into 2488 digested with NcoI and NdeI.	This study
2490 pB506 pET28a Lifeact E17K-MBP-His-Flag	The Lifeact E17K-encoding sequence was generated by annealing oligonucleotides catgggtgtcgcagatttgatcaagaaattcgaaagcatctcaaaggaaaaagg and taccttttttcctttgagatgctttcgaatttcttgatcaaatctgcgacacc, and inserting the resulting double-strand DNA into 2488 digested with NcoI and NdeI.	This study

2491 pB524 pET28a Lifeact E16R-MBP-His-Flag	The Lifeact E16R-encoding sequence was generated by annealing oligonucleotides catgggtgtcgcagatttgatcaagaaattcgaaagcatctcaaagcgtgaagg and taccttcacgctttgagatgctttcgaatttcttgatcaaatctgcgacacc, and inserting the resulting double-strand DNA into 2488 digested with NcoI and NdeI.	This study
565 pET19b-TcdA1	6x His-tagged TcdA1 under control of a T7 promoter	(Gatsogiannis et al., 2018)
613 pET28a-TcdB2-TccC3	6x His-tagged TcdB2-TccC3 fusion under control of a T7 promoter	(Gatsogiannis et al., 2016)
579 pET19b-TccC3HVR	6x His-tagged TccC3(679–960) under control of a T7 promoter	(Roderer et al., 2019)
Plasmids for protein expression in mammalian cells		
693 pDEST Lifeact-mCherry	WT Lifeact-mCherry under a CMV promoter	(Smyth et al., 2012)
2492 pB514 pDEST Lifeact F10A-mCherry	To obtain the F10A mutation in Lifeact, the SalI/BamHI fragment of 693 containing WT Lifeact was replaced by a double stranded DNA fragment that was generated by annealing oligonucleotides tcgactggatcatgggcgtggccgacctgatcaagaaggccgagagcatcagcaaggaggagtcgag atatctagacccagctttcttgtacaaagtggttcgatgg and gatcccatcgaaccactttgtacaagaaagctgggtctagatatctcgactcctccttgctgatgctctcggc cttcttgatcaggtcggccacgcccatgatccag.	This study
2493 pB515 pDEST Lifeact E17K-mCherry	To obtain the E17K mutation in Lifeact, the SalI/BamHI fragment of 693 containing WT Lifeact was replaced by a double stranded DNA fragment that was generated by annealing oligonucleotides tcgactggatcatgggcgtggccgacctgatcaagaagttcgagagcatcagcaaggagaaatcgagat atctagacccagctttcttgtacaaagtggttcgatgg and gatcccatcgaaccactttgtacaagaaagctgggtctagatatctcgatttctccttgctgatgctctcgaa cttcttgatcaggtcggccacgcccatgatccag.	This study
mCherry-Actin-C-18	mCherry-actin under a CMV promoter	(Rizzo et al., 2009)

548

549

References

Aizawa, H., Sameshima, M., Yahara, I., 1997. A green fluorescent protein-actin fusion protein dominantly inhibits cytokinesis, cell spreading, and locomotion in Dictyostelium. Cell Struct Funct 22, 335–345. doi:10.1247/csf.22.335

Ballestrem, C., Wehrle-Haller, B., Imhof, B.A., 1998. Actin dynamics in living mammalian cells. J Cell Sci 111 (Pt 12), 1649–1658.

Belin, B.J., Goins, L.M., Mullins, R.D., 2014. Comparative analysis of tools for live cell imaging of actin network architecture. Bioarchitecture 4, 189–202. doi:10.1080/19490992.2014.1047714

Belyy, A., Raoux-Barbot, D., Saveanu, C., Namane, A., Ogryzko, V., Worpenberg, L., David, V., Henriot, V., Fellous, S., Merrifield, C., Assayag, E., Ladant, D., Renault, L., Mechold, U., 2016. Actin activates Pseudomonas aeruginosa ExoY nucleotidyl cyclase toxin and ExoY-like effector domains from MARTX toxins. Nat Commun 7, 13582. doi:10.1038/ncomms13582

Belyy, A., Santecchia, I., Renault, L., Bourigault, B., Ladant, D., Mechold, U., 2018. The extreme C terminus of the Pseudomonas aeruginosa effector ExoY is crucial for binding to its eukaryotic activator, F-actin. J Biol Chem 293, 19785–19796. doi:10.1074/jbc.RA118.003784

Belyy, A., Tabakova, I., Lang, A.E., Jank, T., Belyi, Y., Aktories, K., 2015. Roles of Asp179 and Glu270 in ADP-Ribosylation of Actin by Clostridium perfringens Iota Toxin. PLoS One 10, e0145708.

Bubb, M.R., Spector, I., Beyer, B.B., Fosen, K.M., 2000. Effects of jasplakinolide on the kinetics of actin polymerization. An explanation for certain in vivo observations. J Biol Chem 275, 5163–5170. doi:10.1074/jbc.275.7.5163

Burkel, B.M., Dassow, von, G., Bement, W.M., 2007. Versatile fluorescent probes for actin filaments based on the actin-binding domain of utrophin. Cell Motil Cytoskeleton 64, 822–832. doi:10.1002/cm.20226

Carlier, M.F., Laurent, V., Santolini, J., Melki, R., Didry, D., Xia, G.X., Hong, Y., Chua, N.H., Pantaloni, D., 1997. Actin depolymerizing factor (ADF/cofilin) enhances the rate of filament turnover: implication in actin-based motility. J Cell Biol 136, 1307–1322. doi:10.1083/jcb.136.6.1307

Coulton, A., Lehrer, S.S., Geeves, M.A., 2006. Functional homodimers and heterodimers of recombinant smooth muscle tropomyosin. Biochemistry 45, 12853–12858. doi:10.1021/bi0613224

Courtemanche, N., Pollard, T.D., Chen, Q., 2016. Avoiding artefacts when counting polymerized actin in live cells with LifeAct fused to fluorescent proteins. Nat Cell Biol 18, 676–683. doi:10.1038/ncb3351

Crews, P., Manes, L.V., Boehler, M., 1986. Jasplakinolide, a cyclodepsipeptide from the marine sponge, Jaspis SP. Tetrahedron Letters 27, 2797–2800. doi:https://doi.org/10.1016/S0040-4039(00)84645-6

Croll, T.I., 2018. ISOLDE: a physically realistic environment for model building into low-resolution electron-density maps. Acta Crystallogr D Struct Biol 74, 519–530. doi:10.1107/S2059798318002425

593 Dancker, P., Low, I., Hasselbach, W., Wieland, T., 1975. Interaction of actin with phalloidin:
594 polymerization and stabilization of F-actin. Biochim Biophys Acta 400, 407–414.
595 doi:10.1016/0005-2795(75)90196-8

596 Daniel Gietz, R., Woods, R.A., 2002. Transformation of yeast by lithium acetate/single-
597 stranded carrier DNA/polyethylene glycol method, in: Guthrie, C., Fink, G.R. (Eds.),
598 Guide to Yeast Genetics and Molecular and Cell Biology - Part B, Methods in
599 Enzymology. Academic Press, pp. 87–96.

600 DiMaio, F., Song, Y., Li, X., Brunner, M.J., Xu, C., Conticello, V., Egelman, E., Marlovits,
601 T.C., Cheng, Y., Baker, D., 2015. Atomic-accuracy models from 4.5-Å cryo-electron
602 microscopy data with density-guided iterative local refinement. Nat Methods 12, 361–
603 365.

604 Ecken, von der, J., Heissler, S.M., Pathan-Chhatbar, S., Manstein, D.J., Raunser, S., 2016.
605 Cryo-EM structure of a human cytoplasmic actomyosin complex at near-atomic
606 resolution. Nature 534, 724–728. doi:10.1038/nature18295

607 Ecken, von der, J., Muller, M., Lehman, W., Manstein, D.J., Penczek, P.A., Raunser, S., 2015.
608 Structure of the F-actin-tropomyosin complex. Nature 519, 114–117.
609 doi:10.1038/nature14033

610 Emsley, P., Lohkamp, B., Scott, W.G., Cowtan, K., 2010. Features and development of Coot.
611 Acta Crystallogr D Biol Crystallogr 66, 486–501. doi:10.1107/S0907444910007493

612 Fleishman, S.J., Leaver-Fay, A., Corn, J.E., Strauch, E.-M., Khare, S.D., Koga, N., Ashworth,
613 J., Murphy, P., Richter, F., Lemmon, G., Meiler, J., Baker, D., 2011. RosettaScripts: a
614 scripting language interface to the Rosetta macromolecular modeling suite. PLoS One 6,
615 e20161.

616 Flores, L.R., Keeling, M.C., Zhang, X., Sliogeryte, K., Gavara, N., 2019. Lifeact-GFP alters
617 F-actin organization, cellular morphology and biophysical behaviour. Sci Rep 9, 3241.
618 doi:10.1038/s41598-019-40092-w

619 Gatsogiannis, C., Merino, F., Prumbaum, D., Roderer, D., Leidreiter, F., Meusch, D.,
620 Raunser, S., 2016. Membrane insertion of a Tc toxin in near-atomic detail. Nat Struct Mol
621 Biol 23, 884–890. doi:10.1038/nsmb.3281

622 Gatsogiannis, C., Merino, F., Roderer, D., Balchin, D., Schubert, E., Kuhlee, A., Hayer-Hartl,
623 M., Raunser, S., 2018. Tc toxin activation requires unfolding and refolding of a β-
624 propeller. Nature 563, 209–213. doi:10.1038/s41586-018-0556-6

625 Hsiao, J.Y., Goins, L.M., Petek, N.A., Mullins, R.D., 2015. Arp2/3 complex and cofilin
626 modulate binding of tropomyosin to branched actin networks. Curr Biol 25, 1573–1582.
627 doi:10.1016/j.cub.2015.04.038

628 Kost, B., Spielhofer, P., Chua, N.H., 1998. A GFP-mouse talin fusion protein labels plant
629 actin filaments in vivo and visualizes the actin cytoskeleton in growing pollen tubes. Plant
630 J 16, 393–401. doi:10.1046/j.1365-313x.1998.00304.x

631 Kumari, A., Kesarwani, S., Javoor, M.G., Vinothkumar, K.R., Sirajuddin, M., 2019.
632 Structural insights into filament recognition by cellular actin markers. bioRxiv.
633 doi:10.1101/846337

634 Kushnirov, V.V., 2000. Rapid and reliable protein extraction from yeast. Yeast 16, 857–860.
635 doi:10.1002/1097-0061(20000630)16:9<857::AID-YEA561>3.0.CO;2-B

636 Lang, A.E., Schmidt, G., Schlosser, A., Hey, T.D., Larrinua, I.M., Sheets, J.J., Mannherz,
637 H.G., Aktories, K., 2010. Photorhabdus luminescens toxins ADP-ribosylate actin and
638 RhoA to force actin clustering. Science 327, 1139–1142. doi:10.1126/science.1184557

639 Liebschner, D., Afonine, P.V., Baker, M.L., Bunkoczi, G., Chen, V.B., Croll, T.I., Hintze, B.,
640 Hung, L.W., Jain, S., McCoy, A.J., Moriarty, N.W., Oeffner, R.D., Poon, B.K., Prisant,
641 M.G., Read, R.J., Richardson, J.S., Richardson, D.C., Sammito, M.D., Sobolev, O.V.,
642 Stockwell, D.H., Terwilliger, T.C., Urzhumtsev, A.G., Videau, L.L., Williams, C.J.,
643 Adams, P.D., 2019. Macromolecular structure determination using X-rays, neutrons and
644 electrons: recent developments in Phenix. Acta Crystallogr D Struct Biol 75, 861–877.
645 doi:10.1107/S2059798319011471

646 Lin, A.Y., Prochniewicz, E., James, Z.M., Svensson, B., Thomas, D.D., 2011. Large-scale
647 opening of utrophin's tandem calponin homology (CH) domains upon actin binding by an
648 induced-fit mechanism. Proc Natl Acad Sci U S A 108, 12729–12733.
649 doi:10.1073/pnas.1106453108

650 Lopata, A., Hughes, R., Tiede, C., Heissler, S.M., Sellers, J.R., Knight, P.J., Tomlinson, D.,
651 Peckham, M., 2018. Affimer proteins for F-actin: novel affinity reagents that label F-actin
652 in live and fixed cells. Sci Rep 8, 6572. doi:10.1038/s41598-018-24953-4

653 Lynen, F., Wieland, U., 1938. Über die Giftstoffe des Knollenblätterpilzes. IV. Justus Liebigs
654 Annalen der Chemie 533, 93–117. doi:10.1002/jlac.19385330105

655 Melak, M., Plessner, M., Grosse, R., 2017. Actin visualization at a glance. J Cell Sci 130,
656 525–530. doi:10.1242/jcs.189068

657 Mentes, A., Huehn, A., Liu, X., Zwolak, A., Dominguez, R., Shuman, H., Ostap, E.M.,
658 Sindelar, C.V., 2018. High-resolution cryo-EM structures of actin-bound myosin states
659 reveal the mechanism of myosin force sensing. Proc Natl Acad Sci U S A 115, 1292–
660 1297. doi:10.1073/pnas.1718316115

661 Merino, F., Pospich, S., Funk, J., Wagner, T., Kullmer, F., Arndt, H.-D., Bieling, P., Raunser,
662 S., 2018a. Structural transitions of F-actin upon ATP hydrolysis at near-atomic resolution
663 revealed by cryo-EM. Nat Struct Mol Biol 25, 528–537. doi:10.1038/s41594-018-0074-0

664 Merino, F., Pospich, S., Funk, J., Wagner, T., Kullmer, F., Arndt, H.-D., Bieling, P., Raunser,
665 S., 2018b. Structural transitions of F-actin upon ATP hydrolysis at near-atomic resolution
666 revealed by cryo-EM. Nat Struct Mol Biol 25, 528–537. doi:10.1038/s41594-018-0074-0

667 Montes-Rodriguez, A., Kost, B., 2017. Direct Comparison of the Performance of Commonly
668 Employed In Vivo F-actin Markers (Lifeact-YFP, YFP-mTn and YFP-FABD2) in
669 Tobacco Pollen Tubes. Front Plant Sci 8, 1349. doi:10.3389/fpls.2017.01349

670 Moriarty, N.W., Grosse-Kunstleve, R.W., Adams, P.D., 2009. electronic Ligand Builder and
671 Optimization Workbench (eLBOW): a tool for ligand coordinate and restraint generation.
672 Acta Crystallogr D Biol Crystallogr 65, 1074–1080. doi:10.1107/S0907444909029436

673 Moriya, T., Saur, M., Stabrin, M., Merino, F., Voicu, H., Huang, Z., Penczek, P.A., Raunser,
674 S., Gatsogiannis, C., 2017. High-resolution Single Particle Analysis from Electron Cryo-
675 microscopy Images Using SPHIRE. J Vis Exp. doi:10.3791/55448

676 Munsie, L.N., Caron, N., Desmond, C.R., Truant, R., 2009. Lifeact cannot visualize some
677 forms of stress-induced twisted F-actin. Nat Methods 6, 317. doi:10.1038/nmeth0509-317

678 Nagasaki, A., T Kijima, S., Yumoto, T., Imaizumi, M., Yamagishi, A., Kim, H., Nakamura,
679 C., Q P Uyeda, T., 2017. The Position of the GFP Tag on Actin Affects the Filament
680 Formation in Mammalian Cells. Cell Struct Funct 42, 131–140. doi:10.1247/csf.17016

Peisker, K., Braun, D., Wolfle, T., Hentschel, J., Funfschilling, U., Fischer, G., Sickmann, A., Rospert, S., 2008. Ribosome-associated complex binds to ribosomes in close proximity of Rpl31 at the exit of the polypeptide tunnel in yeast. Mol Biol Cell 19, 5279–5288. doi:10.1091/mbc.e08-06-0661

Pettersen, E.F., Goddard, T.D., Huang, C.C., Couch, G.S., Greenblatt, D.M., Meng, E.C., Ferrin, T.E., 2004. UCSF Chimera--a visualization system for exploratory research and analysis. J Comput Chem 25, 1605–1612. doi:10.1002/jcc.20084

Pollard, T.D., Cooper, J.A., 2009. Actin, a central player in cell shape and movement. Science 326, 1208–1212. doi:10.1126/science.1175862

Pospich, S., Merino, F., Raunser, S., 2019. Structural effects and functional implications of phalloidin and jasplakinolide binding to actin filaments. bioRxiv. doi:10.1101/794495

Riedl, J., Crevenna, A.H., Kessenbrock, K., Yu, J.H., Neukirchen, D., Bista, M., Bradke, F., Jenne, D., Holak, T.A., Werb, Z., Sixt, M., Wedlich-Soldner, R., 2008. Lifeact: a versatile marker to visualize F-actin. Nat Methods 5, 605–607. doi:10.1038/nmeth.1220

Riedl, J., Flynn, K.C., Raducanu, A., Gartner, F., Beck, G., Bosl, M., Bradke, F., Massberg, S., Aszodi, A., Sixt, M., Wedlich-Soldner, R., 2010. Lifeact mice for studying F-actin dynamics. Nat Methods 7, 168–169. doi:10.1038/nmeth0310-168

Rizzo, M.A., Rizzo, M.A., Davidson, M.W., Davidson, M.W., Piston, D.W., Piston, D.W., 2009. Fluorescent Protein Tracking and Detection: Fluorescent Protein Structure and Color Variants. Cold Spring Harbor Protocols 2009, pdb.top63–pdb.top63. doi:10.1101/pdb.top63

Roderer, D., Schubert, E., Sitsel, O., Raunser, S., 2019. Towards the application of Tc toxins as a universal protein translocation system. Nat Commun 10, 5263. doi:10.1038/s41467-019-13253-8

Sanders, T.A., Llagostera, E., Barna, M., 2013. Specialized filopodia direct long-range transport of SHH during vertebrate tissue patterning. Nature 497, 628–632. doi:10.1038/nature12157

Schiavon, C., Zhang, T., Zhao, B., Andrade, L., Wu, M., Sung, T.-C., Dayn, Y., Feng, J.W., Quintero, O.A., Grosse, R., Manor, U., 2019. Actin chromobody imaging reveals sub-organellar actin dynamics. bioRxiv. doi:10.1101/639278

Schindelin, J., Arganda-Carreras, I., Frise, E., Kaynig, V., Longair, M., Pietzsch, T., Preibisch, S., Rueden, C., Saalfeld, S., Schmid, B., Tinevez, J.-Y., White, D.J., Hartenstein, V., Eliceiri, K., Tomancak, P., Cardona, A., 2012. Fiji: an open-source platform for biological-image analysis. Nat Methods 9, 676–682. doi:10.1038/nmeth.2019

Sheahan, M.B., Staiger, C.J., Rose, R.J., McCurdy, D.W., 2004. A green fluorescent protein fusion to actin-binding domain 2 of Arabidopsis fimbrin highlights new features of a dynamic actin cytoskeleton in live plant cells. Plant Physiol 136, 3968–3978. doi:10.1104/pp.104.049411

Sliogeryte, K., Thorpe, S.D., Wang, Z., Thompson, C.L., Gavara, N., Knight, M.M., 2016. Differential effects of LifeAct-GFP and actin-GFP on cell mechanics assessed using micropipette aspiration. J Biomech 49, 310–317. doi:10.1016/j.jbiomech.2015.12.034

Smyth, J.W., Vogan, J.M., Buch, P.J., Zhang, S.-S., Fong, T.S., Hong, T.-T., Shaw, R.M., 2012. Actin cytoskeleton rest stops regulate anterograde traffic of connexin 43 vesicles to the plasma membrane. Circ Res 110, 978–989. doi:10.1161/CIRCRESAHA.111.257964

726 Spracklen, A.J., Fagan, T.N., Lovander, K.E., Tootle, T.L., 2014. The pros and cons of
727 common actin labeling tools for visualizing actin dynamics during Drosophila oogenesis.
728 Dev Biol 393, 209–226. doi:10.1016/j.ydbio.2014.06.022

729 Tanaka, K., Takeda, S., Mitsuoka, K., Oda, T., Kimura-Sakiyama, C., Maéda, Y., Narita, A.,
730 2018. Structural basis for cofilin binding and actin filament disassembly. Nat Commun 9,
731 1860.

732 Wagner, T., Merino, F., Stabrin, M., Moriya, T., Antoni, C., Apelbaum, A., Hagel, P., Sitsel,
733 O., Raisch, T., Prumbaum, D., Quentin, D., Roderer, D., Tacke, S., Siebolds, B.,
734 Schubert, E., Shaikh, T.R., Lill, P., Gatsogiannis, C., Raunser, S., 2019. SPHIRE-
735 crYOLO is a fast and accurate fully automated particle picker for cryo-EM. Commun
736 Biol 2, 218. doi:10.1038/s42003-019-0437-z

737 Wang, R.Y.-R., Kudryashev, M., Li, X., Egelman, E.H., Basler, M., Cheng, Y., Baker, D.,
738 DiMaio, F., 2015. De novo protein structure determination from near-atomic-resolution
739 cryo-EM maps. Nat Methods 12, 335–338.

740 Zivanov, J., Nakane, T., Forsberg, B.O., Kimanius, D., Hagen, W.J., Lindahl, E., Scheres,
741 S.H., 2018. New tools for automated high-resolution cryo-EM structure determination in
742 RELION-3. Elife 7.

743

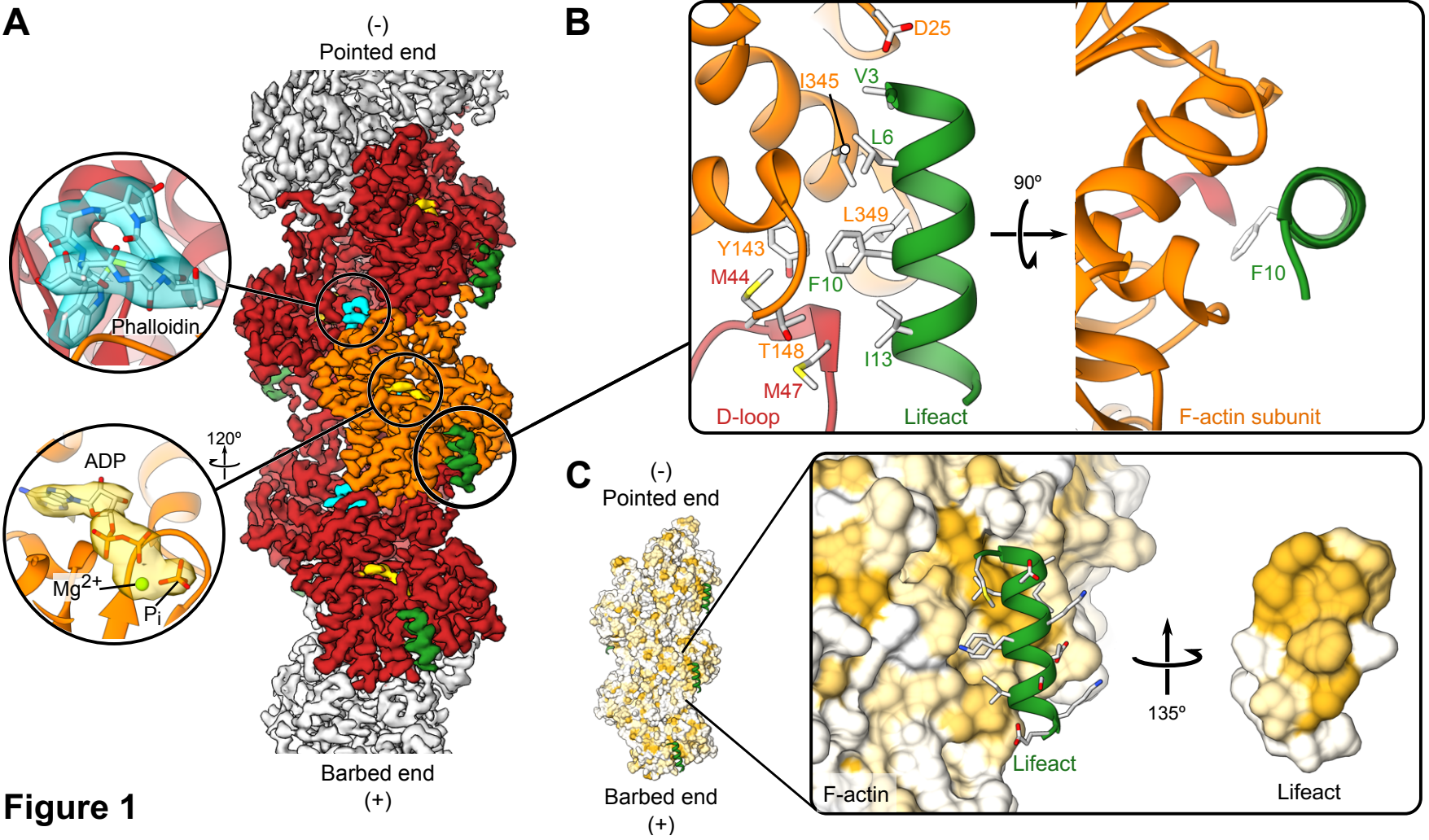
A
(-)
Pointed end
Phalloidin
ADP
120°
Mg2+
Pi
Barbed end
(+)
B
D25
I345
V3
L6
L349
Y143
M44
F10
T148
M47
I13
D-loop
Lifeact
90°
F10
F-actin subunit
C
(-)
Pointed end
Barbed end
(+)
F-actin
Lifeact
135°
Lifeact

Figure 1

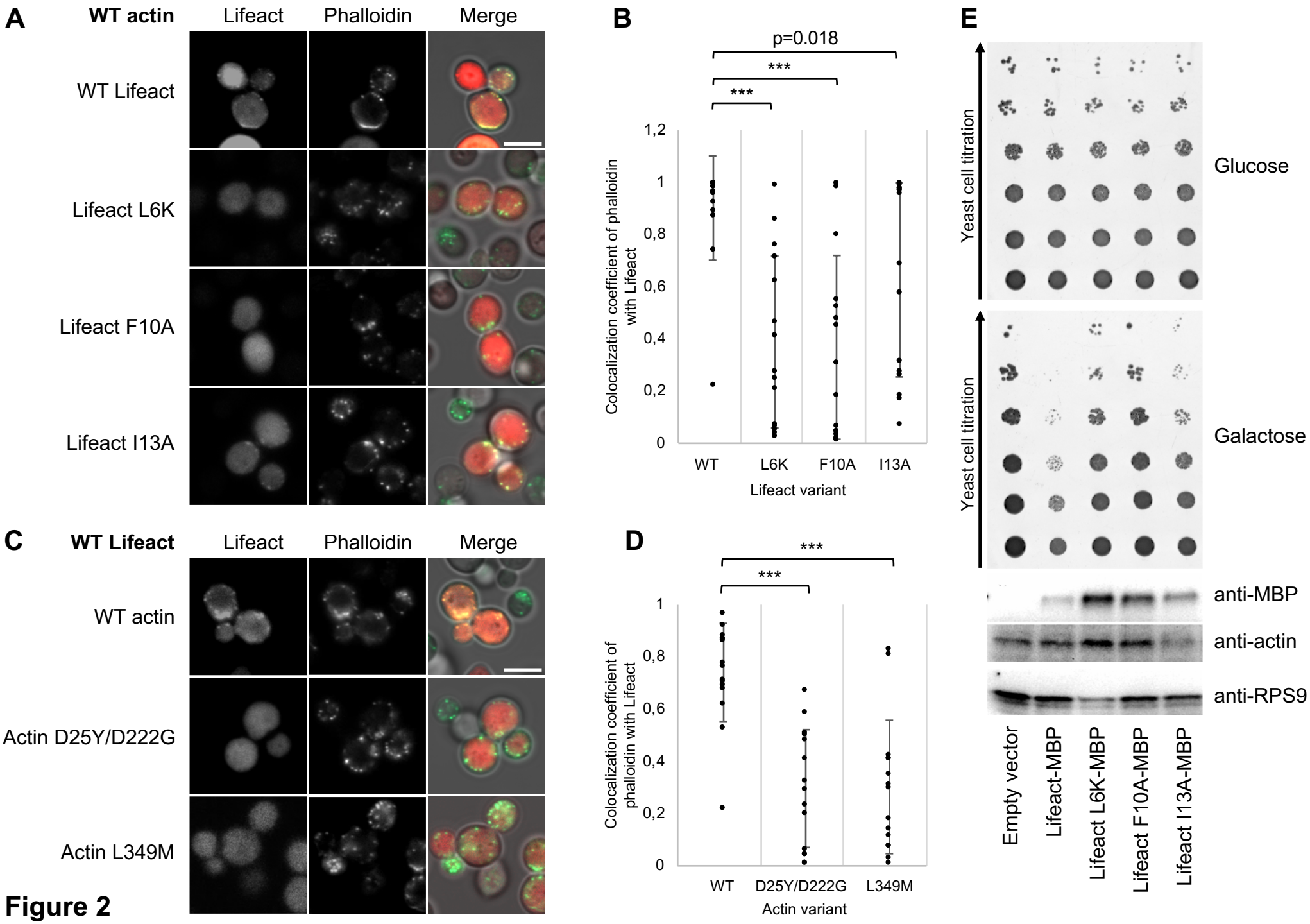
A
WT actin
Lifeact
Phalloidin
Merge
WT Lifeact
Lifeact L6K
Lifeact F10A
Lifeact I13A
B
p=0.018
***
***
Colocalization coefficient of phalloidin with Lifeact
1,2
1
0,8
0,6
0,4
0,2
0
WT
L6K
F10A
I13A
Lifeact variant
C
WT Lifeact
Lifeact
Phalloidin
Merge
WT actin
Actin D25Y/D222G
Actin L349M
D
***
***
Colocalization coefficient of phalloidin with Lifeact
1
0,8
0,6
0,4
0,2
0
WT
D25Y/D222G
L349M
Actin variant
E
Yeast cell titration
Glucose
Yeast cell titration
Galactose
anti-MBP
anti-actin
anti-RPS9
Empty vector
Lifeact-MBP
Lifeact L6K-MBP
Lifeact F10A-MBP
Lifeact I13A-MBP

Figure 2

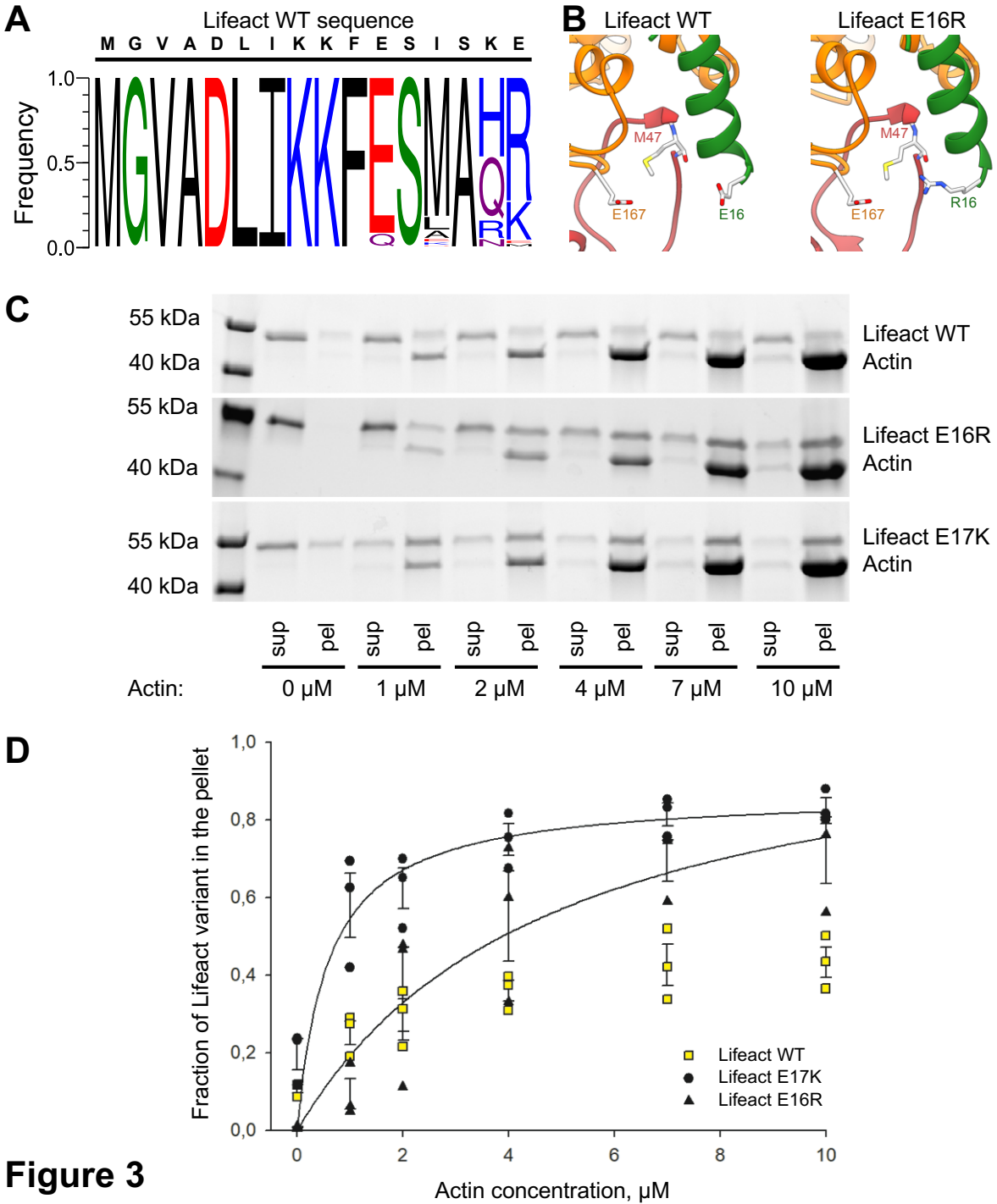
A
Lifeact WT sequence
M G V A D L I K K F E S I S K E
Frequency
1.0
0.5
0.0
B
Lifeact WT
Lifeact E16R
M47
E167
E16
R16
C
55 kDa
40 kDa
Lifeact WT
Actin
Lifeact E16R
Actin
Lifeact E17K
Actin
sup
pel
Actin:
0 µM
1 µM
2 µM
4 µM
7 µM
10 µM
D
Fraction of Lifeact variant in the pellet
1,0
0,8
0,6
0,4
0,2
0,0
0
2
4
6
8
10
Actin concentration, µM
Lifeact WT
Lifeact E17K
Lifeact E16R

Figure 3

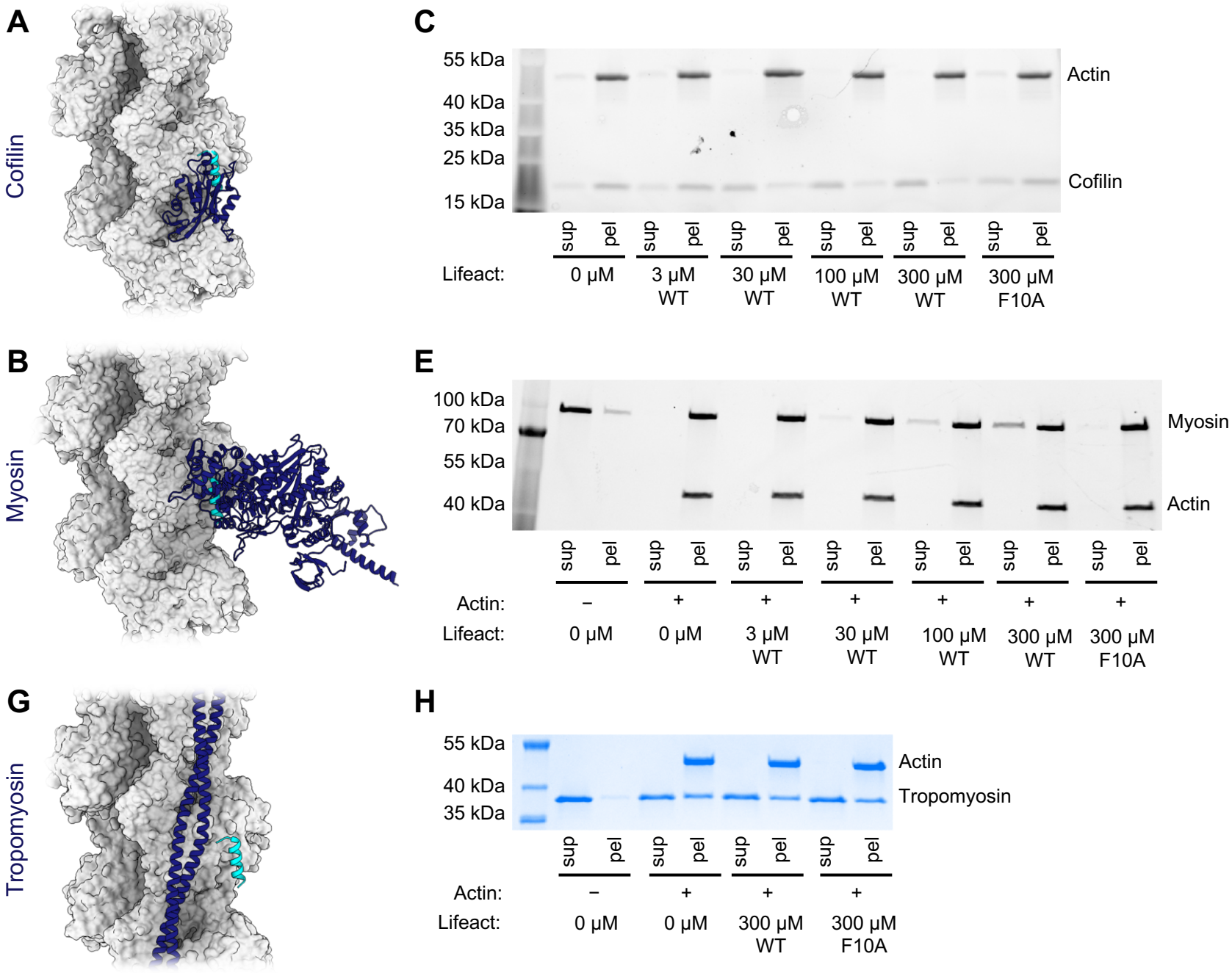
A
Cofilin
B
Myosin
G
Tropomyosin
C
55 kDa
40 kDa
35 kDa
25 kDa
15 kDa
Actin
Cofilin
sup
pel
Lifeact:
0 μM
3 μM WT
30 μM WT
100 μM WT
300 μM WT
300 μM F10A
D
Fraction of cofilin in the pellet
Lifeact WT
Lifeact F10A
Lifeact concentration, μM
E
100 kDa
70 kDa
55 kDa
40 kDa
Myosin
Actin
Actin:
Lifeact:
F
Fraction of myosin in the pellet
H
55 kDa
40 kDa
35 kDa
Actin
Tropomyosin
I
Fraction of tropomyosin in the pellet
No actin
No Lifeact
No Lifeact
300 μM Lifeact WT
300 μM Lifeact F10A

Figure 4

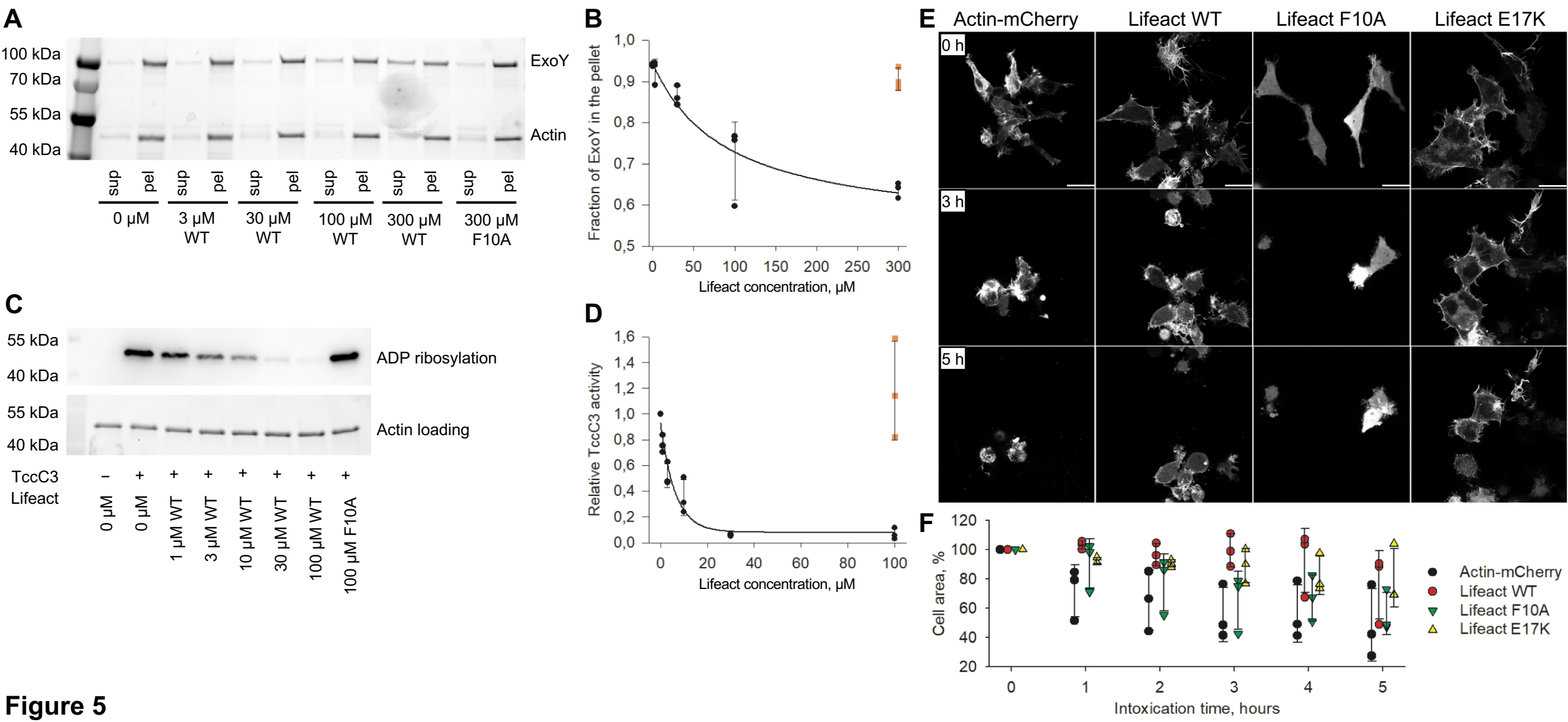
A
100 kDa
70 kDa
55 kDa
40 kDa
ExoY
Actin
sup
pel
0 µM
3 µM WT
30 µM WT
100 µM WT
300 µM WT
300 µM F10A
B
Fraction of ExoY in the pellet
Lifeact concentration, µM
C
55 kDa
40 kDa
ADP ribosylation
Actin loading
TccC3
Lifeact
0 µM
1 µM WT
3 µM WT
10 µM WT
30 µM WT
100 µM WT
100 µM F10A
D
Relative TccC3 activity
Lifeact concentration, µM
E
Actin-mCherry
Lifeact WT
Lifeact F10A
Lifeact E17K
0 h
3 h
5 h
F
Cell area, %
Intoxication time, hours
Actin-mCherry
Lifeact WT
Lifeact F10A
Lifeact E17K

Figure 5

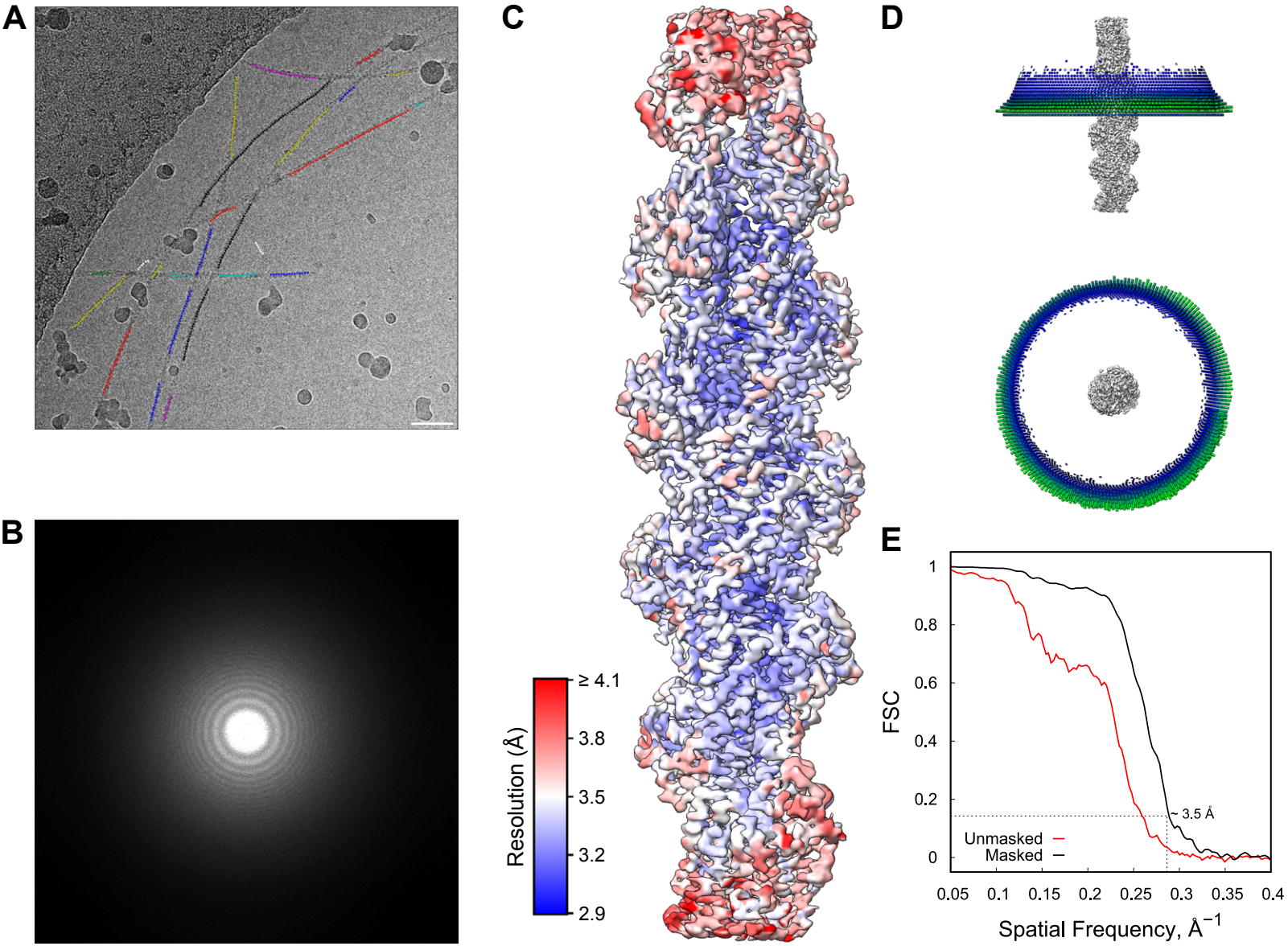
A
B
C
D
E
Resolution (Å)
≥ 4.1
3.8
3.5
3.2
2.9
FSC
1
0.8
0.6
0.4
0.2
0
3.5 Å
Unmasked
Masked
0.05
0.1
0.15
0.2
0.25
0.3
0.35
0.4
Spatial Frequency, Å^{-1}

Figure S1

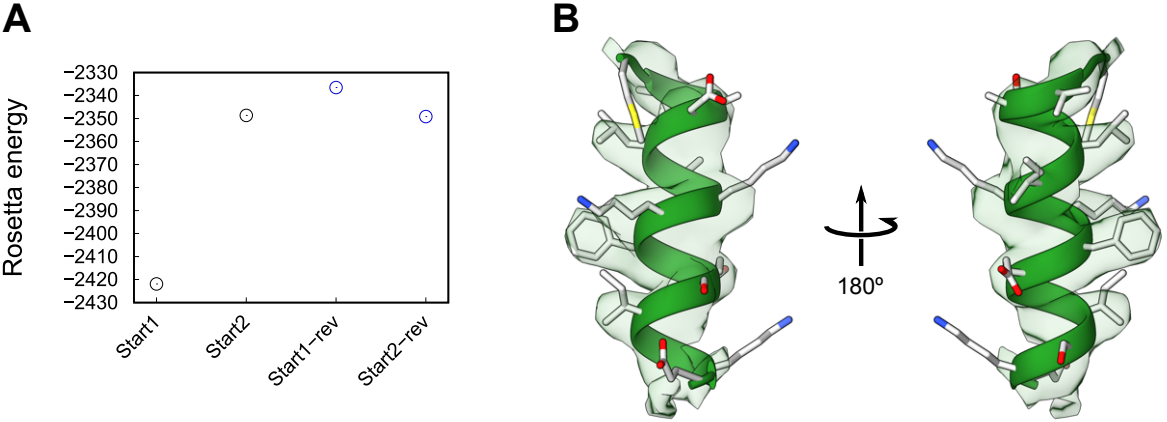
A
Rosetta energy
−2330
−2340
−2350
−2360
−2370
−2380
−2390
−2400
−2410
−2420
−2430
Start1
Start2
Start1−rev
Start2−rev
B
180°

Figure S2

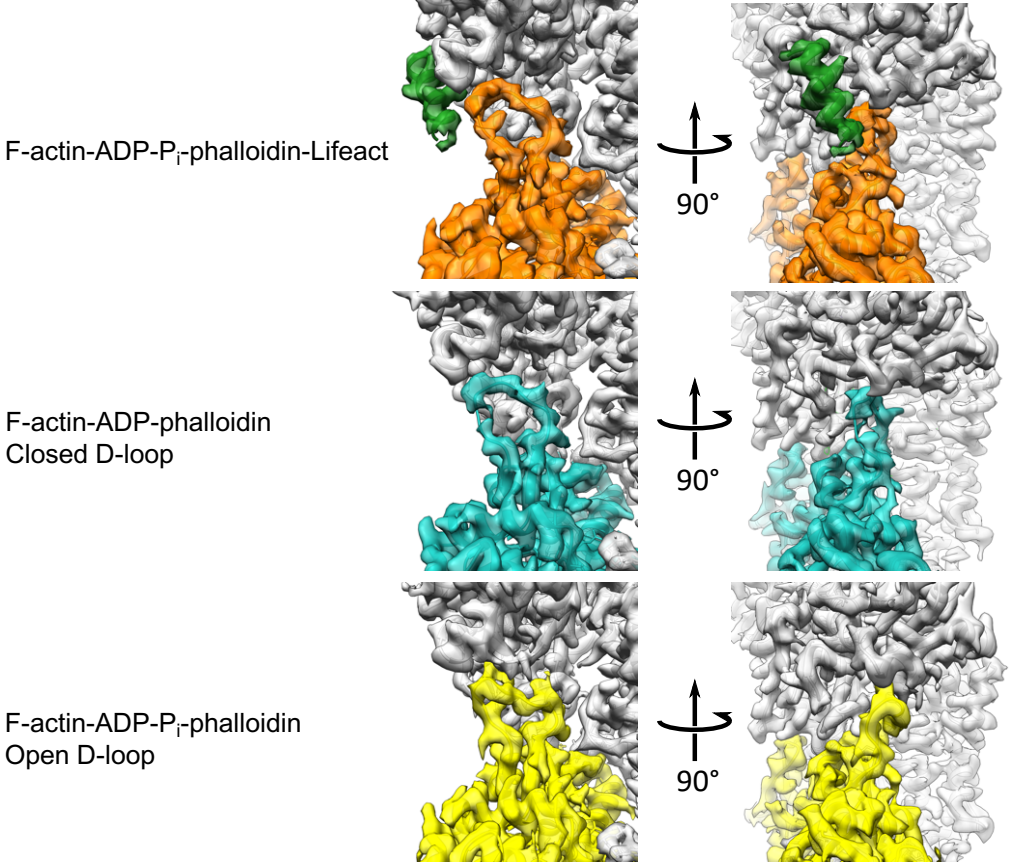
F-actin-ADP-Pi-phalloidin-Lifeact
90°
F-actin-ADP-phalloidin
Closed D-loop
90°
F-actin-ADP-Pi-phalloidin
Open D-loop
90°

Figure S3